Hindawi
Advances in Civil Engineering
Volume 2020, Article ID 1520278, 25 pages
https://doi.org/10.1155/2020/1520278

Research Article

Investigation on Flooding-Resistant Performance of Integral Abutment and Jointless Bridge

Yizhou Zhuang,[1] Keyao Wu,[1] Liang Xu,[2] Huihui Li,[3] Diego Maria Barbieri,[4] and Zhumei Fu[5]

[1]*College of Civil and Architectural Engineering, Zhejiang University of Technology, 18 Chaowang Road, Hangzhou, Zhejiang 310014, China*
[2]*School of Civil Engineering, Chongqing University, 83 Shabei Street, Chongqing 400045, China*
[3]*Department of Civil and Environmental Engineering, The City College of City University of New York, New York 10031, NY, USA*
[4]*Norwegian University of Science and Technology, Department of Civil and Environmental Engineering, Høgskoleringen 7A, Trondheim 7491, Trøndelag, Norway*
[5]*College of Civil Engineering, Fuzhou University, 2 Xueyuan Road, University Town, Fuzhou, Fujian 350108, China*

Correspondence should be addressed to Liang Xu; liangxu360427@cqu.edu.cn

Received 21 August 2019; Revised 27 December 2019; Accepted 4 January 2020; Published 21 February 2020

Academic Editor: Jian Ji

Bridge washouts connected to flood events are deemed one of the main reasons for structural collapse. Compared to traditional continuous jointed bridges, integral abutment and jointless bridges (IAJBs) have better lateral stability because there are no expansion devices. The mechanical performance of Shangban IAJ bridge, located in Fujian, China, is thoroughly investigated by Finite Element Analysis (FEA). The numerical model is created and validated based on experimental results obtained from static load tests performed on the bridge. A detailed parametric analysis is carried out to assess the correlation between the flood-resistant performance and a number of parameters: skew angle, water-blocking area, span number, pile section geometry, and abutment height. Except for the abutment height, other parameters significantly affect the bridge performance. Furthermore, the change in the span number has a meaningful impact only when fewer than four spans are modeled. Finally, pushover analyses estimate the maximum transverse displacement and the sequence of plastic hinge creation as well as the mechanical behaviour of the structure under lateral flood loads. The analysis results show that IAJBs have better flooding-resistant performance than conventional jointed bridges.

1. Introduction

Bridge washouts connected to flood events are deemed one of the main reasons for the collapse of bridge structure [1]. Integral abutment jointless bridges (IAJBs) have better lateral stability and flooding-resistant performance than conventional jointed bridges because expansion devices are elimanted [2]. Expansion joints and movable bearings are eliminated in IAJBs to consolidate the bridge deck, the slab, and the abutment as a whole. Special measures are adopted to tackle temperature-induced deflections [3].

IAJBs are commonly built worldwide thanks to their good stability and integrity. When the length and/or exposed abutment height becomes large, one solution is to use semi-integral abutment details that are suitable for accelerated bridge constructions [4]. However, there is a lack of corresponding research on the flood resistance of IAJBs. Therefore, this study thoroughly investigates the flood-resistant performance of an IAJB. The mechanical behaviour of Shangban Bridge (Fujian, China) is studied numerically by means of Finite Element Analysis (FEA). The model is created by using MIDAS/Civil software based on the

experimental results (vertical reactions of bearings and top displacement of piers) from static load tests performed on the bridge. A detailed parametric analysis is carried out to assess the correlation between the flood-resistant performance and a number of parameters: skew angle, water-blocking area, span number, pile section geometry, and abutment height.

Witzany and Cejka [5] and Ghorbani [1] investigated the erosion and the structural damage connected to floods by comparing several event scenarios. Ko et al. [6] proposed a nonlinear quasi-static analysis procedure for the evaluation of flood-resistant capacity of scoured bridges. Recently, Qeshta [7] proposed a comprehensive vulnerability and resilience assessment method for bridges under extreme wave hazards.

Girton et al. [8] studied the influence of temperature on piles and provided effective theoretical guidance for the design of bridge foundations without expansion joints. Greimann and Wolde-Tinsae [9] and Abendtroth et al. [10] investigated the bearing capacity of pile foundations and proposed two methods for its assessment. Ghalesari et al. [11] performed numerical parametric studies on the differential settlements for a piled raft on undrained soil. Later, Ghalesari et al. [12] also developed a design criterion for piled raft foundations based on settlements, raft bending moment, and pile butt load ratio. Kamel et al. [13] studied the compatibility between an integral abutment bridge without expansion joints and prefabricated prestressed concrete piles. Yalcin [14] investigated the effect of skewness and superstructure-abutment continuity on the distribution of live load effects for skewed integral abutment bridges (SIABs) and skewed simply supported bridges (SSABs). Modarresi et al. [15] proposed a correction to the Randolph and Wroth equation for settlement prediction including soil relative density.

Elastic analyses are generally inadequate to describe the inelastic response of the bridge during flood events [16]. To address this issue, Freeman [17] proposed the pushover analysis method considering the response spectrum of the structure. This approach is referred to as the capacity spectrum method. Pushover analysis is a nonlinear static calculation, which can be used to determine the dynamic characteristics of the structure and estimate the available plastic capacities [18, 19]. Pushover analysis is generally carried out assuming two different control points of the structure [20, 21]. Previous experience highlighted the effectiveness of the methodology [22, 23].

Therefore, this study performs the pushover analysis to assess the transverse maximum displacement of the Shangban Bridge and to examine the order in which plastic hinges occur. The proposed framework used for Shangban Bridge in this study could be extended to other IAJBs as a guide to flood-resistant performance design.

2. Brief Introduction to the Case-Study Bridge

This paper investigates the mechanical behaviour and flood-resistant performance of Shangban Bridge. The structure is the longest IAJB in China and is located in Yong Chun County, Fujian Province. The general features and the dimensions of Shangban Bridge are reported in Figures 1 and 2. The total length of the structure is 137.1 m and the width is 8.5 m. The superstructure is formed by four 30 m prestressed concrete T-shaped girders. Each of the four T-shaped girders is 1.8 m high and 1.56 m wide; the wet cast segment is 0.6 m wide. The double-column piers are 1.5 m in diameter (Figure 3). Given the favorable geological conditions under the bridge, a spread foundation was built. The abutment is 1.2 m high with dense sand as backfill soil. The substructure is composed of four rectangular piles (70×50 cm) arranged in a row to adapt to the deflections caused by temperature changes (Figures 1, 4, and 5). The structural parameters of Shangban Bridge are shown in Table 1 and the height of the columns is shown in Table 2. The steel bars are HPB235, with a yield strength of 235 MPa and elastic modulus of 200 GPa (equivalent to BST420S in Germany) [24].

3. Flood Force Calculation

The flood force acting on Shangban Bridge is calculated for the most unfavorable condition, namely, inundation or submersion of the railing. Figure 6 displays the overall stress distribution acting on one bridge girder. The slab is subjected to the pressure difference between upstream and downstream caused by the flood (Figure 7).

In Figures 6 and 7, B is the width of Shangban Bridge, h is the height of Shangban Bridge, t_1 and t are railing height and girder height, respectively, F_{DP} is the shape resistance, F_{Df} is the friction resistance, F_P is hydrostatic uplift force, and F_L is buoyancy force.

3.1. Horizontal Actions on the Superstructure. The shape resistance is formed by the pressure difference between the upstream and the downstream of the main girder. The distribution is shown on the upstream side of the main girder in Figure 7.

3.1.1. Shape Resistance. Since the upstream surface of the bridge superstructure is perpendicular to the flow direction, the general expression of the flood force F_{DP} is [25]

$$d(F_D)_P = (C_D)_p \frac{\rho v^2}{2} dA, \tag{1}$$

where $(C_D)_P$ is the shape resistance coefficient. According to the formula of differential pressure resistance, $(C_D)_P = 2.1$; dA is the infinitesimal area of the main girder surface; v is the flow velocity at dA; and ρ is the fluid density. By integration of equation (1), F_{DP} can be expressed as

$$\begin{aligned} F_{Dp} &= \iint_{A_1} (C_D)_{p_1} \frac{\rho v^2}{2} \mathrm{d}A + \iint_{A_2} (C_D)_{p_2} \frac{\rho v^2}{2} \mathrm{d}A \\ &= (C_D)_{p_1} \frac{\rho v^2}{2} A_1 + (C_D)_{p_2} \frac{\rho v^2}{2} A_2, \end{aligned} \tag{2}$$

where $(C_D)_{p1}$ and $(C_D)_{p2}$ are the shape resistance coefficient of girder and railing and A_1 and A_2 represent the areas of the girder and railing, respectively.

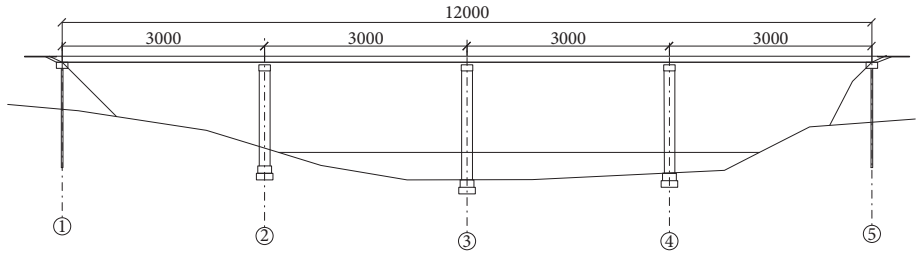

Figure 1: Elevation of Shangban Bridge. (dimensions in cm).

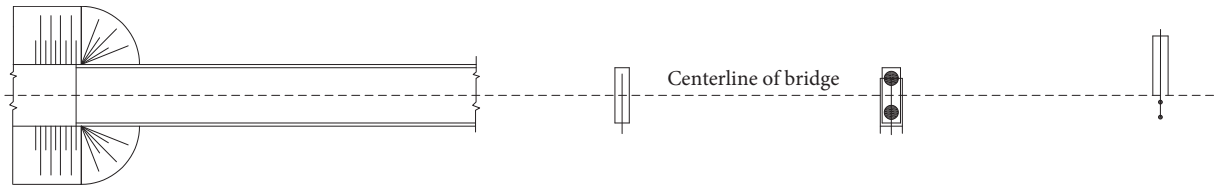

Figure 2: Plan view of Shangban Bridge.

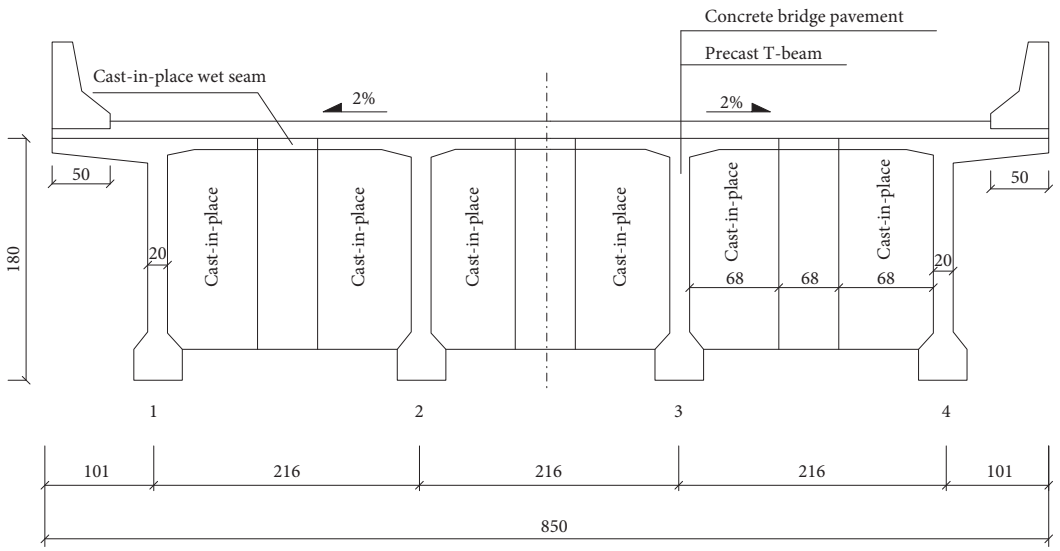

Figure 3: Cross-section of Shangban Bridge (dimensions in cm).

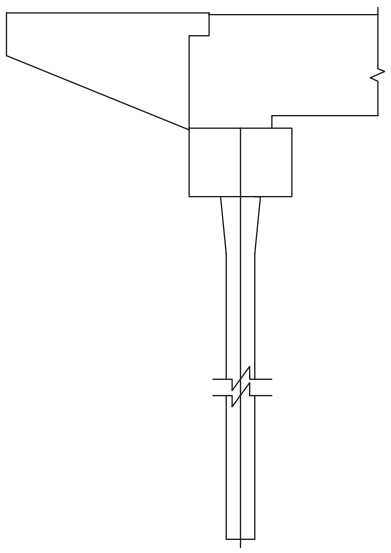

Figure 4: Integral abutment of Shangban Bridge.

Figure 5: Profile of Shangban Bridge.

Table 1: Parameters of Shangban Bridge.

Spans n	Average water depth h (m)	Girder height t (m)	Railing height t_1 (m)	Pier's longitudinal width c (m)	Pier's transverse width d (m)	Abutment height t_2 (m)	Bridge width B (m)	Length L (m)
4	8.6	1.8	1.2	1.5	1.5	1.2	8.5	137.1

Table 2: Height of the columns of Shangban Bridge.

	Column 1	Column 2	Column 3	Column 4	Column 5	Column 6
Height of column (m)	10.65	10.65	12.95	12.95	11.25	11.25

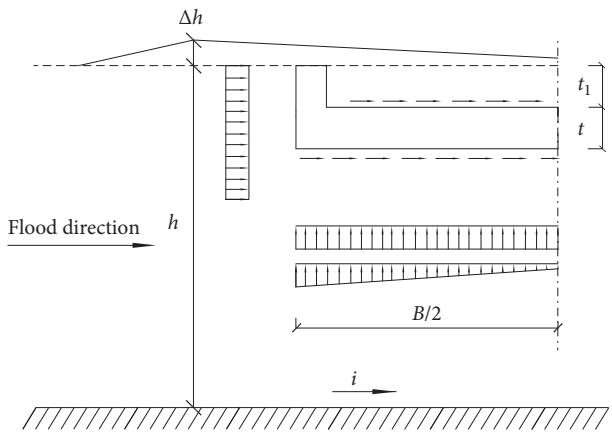

Figure 6: Distribution of flood force.

3.1.2. Friction Resistance. The friction resistance exerted by the surface subject to water flow F_{Df} can be expressed as [25]

$$d(F_D)_f = \tau_{xy} \sin\alpha \, dA,$$
$$\tau_{xy} = \left[1.89 + 1.62 \lg \frac{B}{\varepsilon}\right]^{-2.5} \cdot \frac{1}{2} \cdot \frac{\rho v^2}{2}, \quad (3)$$

where τ_{xy} is the tangential resistive stress on the infinitesimal surface dA, α is the angle between the flow direction and the normal direction of dA, $(C_D)_P$ is the coefficient of frictional resistance, B is the bridge width, and ε is the surface roughness. As a simplification, it is assumed that the flow rates at the beginning and at the end of the girders have the same average velocity. Consequently, the total flood force F_{Df} can be expressed as

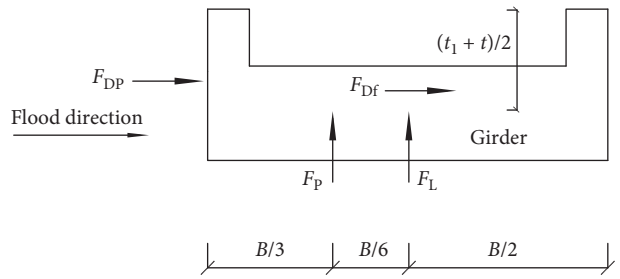

Figure 7: Simplified map of flood force distribution.

$$F_{Df} = \iint_{A_3} (C_D)_{f1} \frac{\rho v^2}{2} dA + \iint_{A_4} (C_D)_{f2} \frac{\rho v^2}{2} dA$$
$$= (C_D)_{f1} \frac{\rho v^2}{2} A_3 + (C_D)_{f2} \frac{\rho v^2}{2} A_4, \quad (4)$$

where $(C_D)_{f1}$ and $(C_D)_{f2}$ are the frictional resistance coefficients at the top and at the bottom of the main girder, respectively, and A_3 and A_4 are the infiltration areas of the top and at the bottom surfaces of the main girder, respectively. Since $(C_D)_{f1} = (C_D)_{f2} = (1.89 + 1.62 \log(B/\varepsilon))^{-2.5}$, $(C_D)_{P1} = (C_D)_{P2} = 2.1$, $A_1 = t$, $A_2 = 2t_1$, and $A_3 = A_4 = B$ and based on equations (2) and (4), the resistance of the unit length of the superstructure is

$$F_D = \left[2\left(1.89 + 1.62 \lg \frac{B}{\varepsilon}\right)^{-2.5} \cdot B + 2.1(t + 2t_1)\right] \frac{\rho v^2}{2}. \quad (5)$$

Equation (5) is derived based on experiments [25]. Therefore, the following correction factors are used to account for adjustments:

$$F_D' = k_1 k_2 k_3 k_4 k_5 F_D, \quad (6)$$

where F_D' is the lateral flood force after being corrected by formula (6). The parameters k_1, k_2, k_3, k_4, and k_5 express the impact and influence of the sediment, the longitudinal slope of the watercourse, the slope of the trench, the flood frequency, and the flood direction, respectively. Among them, k_1, k_2, k_3, and k_4 can be determined according to Xu [25]. The flood direction exerts a very relevant effect on the bridge: the flood force reaches its maximum value when the flow is perpendicular to the bridge centerline, in which case $k_5 = \cos(\alpha) = 1$.

3.2. Vertical Actions on the Superstructure. When the water velocity is constant and the flow is approximately parallel to the bridge, the buoyancy F_L and the hydrostatic uplift F_P forces acting on the bridge can be expressed as

$$F_L = \gamma V_e, \tag{7}$$

$$F_P = \xi A_x \gamma \Delta h, \tag{8}$$

where γ is the specific weight of water, V_e is the drainage volume, ξ is the coefficient of pressure attenuation, A_x is the bottom area of the main girder, and Δh is the water height in front of the bridge. The vertical flood force variates with the fluctuation and the orientation of the water level, which can be directed upward or downward. The calculation takes into account forces directed upward, the most dangerous scenario. Therefore, considering equations (7) and (8), the total vertical force F_S acting on the bridge is

$$F_s = F_L + F_P = \gamma V + \xi A_x \gamma \Delta h. \tag{9}$$

3.3. Actions on Piers. The flow velocity in correspondence of the pier body is assumed to be constant. Figure 8 displays the distribution of the acting forces, where d represents the diameter of the column.

The horizontal forces q acting along the height h can be expressed as

$$q = \frac{dF_D}{dh} = \left[\frac{(C_D)_p}{2} c + (C_D)_f d\right] \rho v^2, \tag{10}$$

where ρ is specific density of water, c is the longitudinal section size of piers, $(C_D)_P$ is the shape resistance coefficient of pier, taken as 2.1, $(C_D)_f$ is the coefficient of frictional resistance of pier, $(C_D)_f = [1.89 + 1.62 \log (B/\varepsilon)]^{-2.5}$, and ε is the surface roughness of pier.

3.4. Overall Actions on Shangban Bridge. The longitudinal slope of the ditch is 10‰, the average slope of the mountain is 20%, and the proportion of muddy water muddy is 1.0.

The horizontal flood force F_D, the vertical flood force F_L and the flood buoyancy are calculated as reported in Sections 3.1 to 3.3. Their values are 69 kN, 35 kN, and 21 kN, respectively; the flood load acting on the piers is 18 kN/m (Table 3).

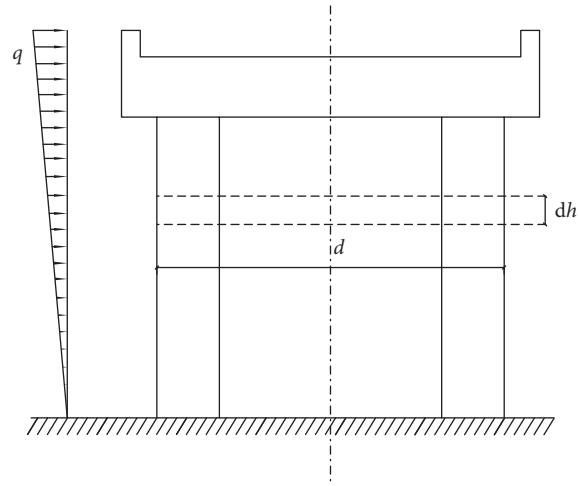

Figure 8: Distribution of flood force on the piers.

Table 3: Values of flood forces on Shangban Bridge.

Average water depth h (m)	F_D (kN)	F_L (kN)	F_P (kN)	q (kN/m)
8.6	69	35	21	18

4. Finite Element Modeling and Validation

4.1. Finite Element Model. The finite element (FE) model of Shangban Bridge is built with a girder grid using MIDAS/Civil software. Girders, piers, and piles are linked together with flexible connections. Pile-soil interaction is simulated with soil springs. The model includes 789 nodes and 1,132 elements (Figure 9). Figure 10 displays a detail of the spring system.

The pile-soil interaction and soil-abutment interaction (see Figure 10) in this model are simulated with soil springs (including a lateral spring, vertical spring, and point spring) and backfill springs, respectively [26–29]. Assuming that the vertical deformation is relatively small, the stiffness of the vertical soil spring and point spring at the bottoms of the piles are simulated by the "m" method, which is calculated from the ratio of the ultimate frictional resistance f_{max} and the corresponding displacement, the bottom limit force q_{max} of piles and their corresponding displacement, respectively [30, 31]. The f_{max} and q_{max} are calculated by theoretical formulas in specifications [32]. The corresponding displacement of the ultimate frictional resistance f_{max} and the bottom limit force q_{max} is 9% of the pile diameter and 8 mm, respectively [31]. The stiffness of the lateral spring and backfill springs are calculated by the p-y method considering complete elastic-plastic constitute of the soil [9].

4.2. Static Load Test. Static field load tests performed on Shangban Bridge are utilized to validate the FE numerical model. The purpose of the tests is to measure the deflections and the strains in the middle and at one-fourth section of the bridge length, as depicted in Figures 11 and 12, to further validate the correctness of the established FEM. Strain

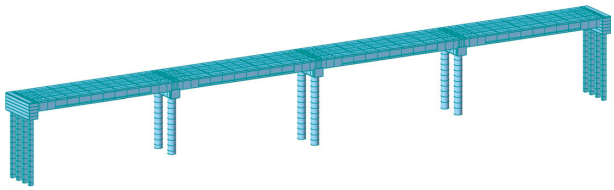

Figure 9: FEM mesh of Shangban Bridge.

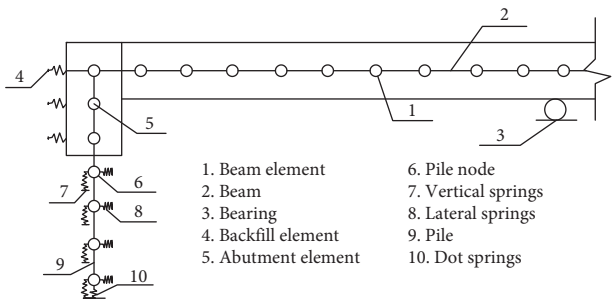

Figure 10: Detail of FEM.

gauges were installed at the bottom of side girder, while deflection meters were installed at the bottom of the middle girder, as depicted in Figure 12.

Two three-axle trucks, with actual weights of 283.4 kN and 296.8 kN, exerted loads on the deck girder at predesigned positions, as shown in Figure 13. This met the requirement of theoretical gross weight defined in the literature [33] of 300 kN. Details of the discrepancy between the actual and ideal loadings are shown in Table 4.

The static load test of Shangban Bridge had two longitudinal vehicle load conditions and three transverse vehicle load conditions, as displayed in Figure 14. The distance from the center line of #1 abutment to the rear axle of the vehicle was 8.9 m and 15 m in longitudinal vehicle load condition I and condition II, respectively. Only one vehicle was used for transverse vehicle load condition 1, where the center line of the outer wheel was 0.5 m away from the guardrail. In transverse vehicle load condition 2, another vehicle was added 1.2 m away from the original vehicle on the basis of the vehicle condition 1. Transverse vehicle load condition 3 kept the number and distance of vehicles in condition 2, but the distance between the center line of the outer wheel and the guardrails was changed from 0.5 m to 1.25 m.

4.3. Validation of Finite Element Model. The data of the static load test are divided into two groups. The first group is used to modify the model, mainly to modify the stiffness of the soil springs and the elastic modulus of the bridge structure in the model. The second group is used to validate the accuracy of the modified model. Specifically, the displacement and strain values obtained from the static load test are compared with the model calculation results.

4.3.1. Comparison between Numerical and Experimental Displacements. Based on the case study on MIDAS/Civil, the accuracy of the FE model can be validated by the static load test results of the bridge. Under each load condition,

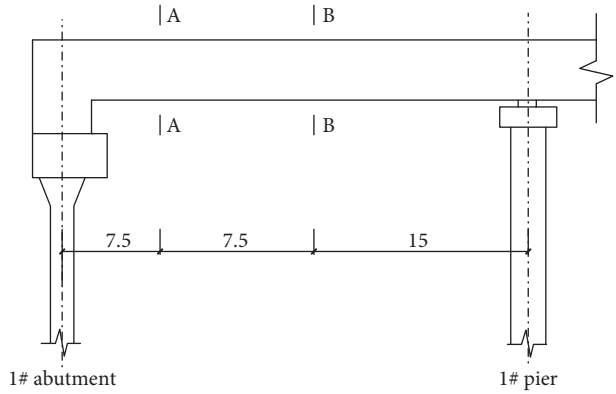

Figure 11: Testing sections.

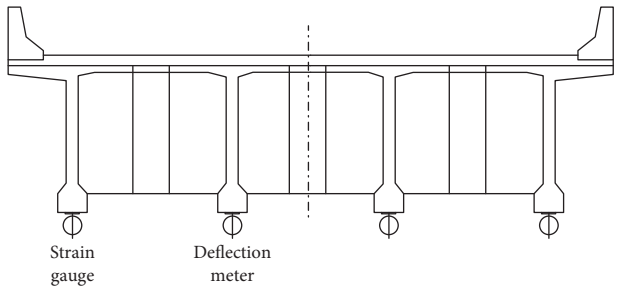

Figure 12: Layout of measuring points.

both the experimental values and numerical values of the deflection of the girder at the one-fourth (A-A) and the middle (B-B) section are shown in Figure 15, where the load condition I-1 represents longitudinal load condition I and lateral vehicle load condition 1 and other states are denoted similarly.

4.3.2. Comparison between Numerical and Experimental Strain Values. Under each load condition, both the numerical and experimental values of the strain of the girder at cross-section (A-A) and cross-section (B-B) are shown in Figure 16. The meaning of each state is the same as in Figure 15.

Because a good agreement is observed between the numerical and the experimental results, the created FE model is considered reliable for the further analyses of the study.

5. Comparison between IAJB and Conventional Bridge

5.1. Analysis of IAJB

5.1.1. Stress Analysis of Superstructure. The minimum transverse displacement between the girder and the pier is 0.073 m obtained from numerical analysis, which is larger than the gap between the girder and the stopper, namely, 0.05 m. This indicates that the transverse movement of the bearings against the flood direction is constrained. In

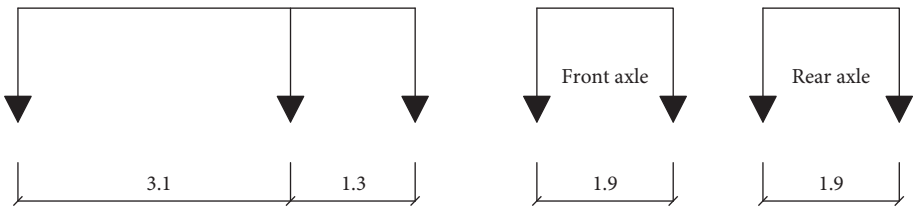

Figure 13: Wheelbase of the vehicles used for static load tests (m).

Table 4: Theoretical and actual weights.

Vehicle number		Front axle weight (kN)	Center and rear axle weight (kN)	Gross weight (kN)
1	Theoretical weight	60	240	300
	Actual weight	60.4	223	283.4
2	Theoretical weight	60	240	300
	Actual weight	54.8	242	296.8

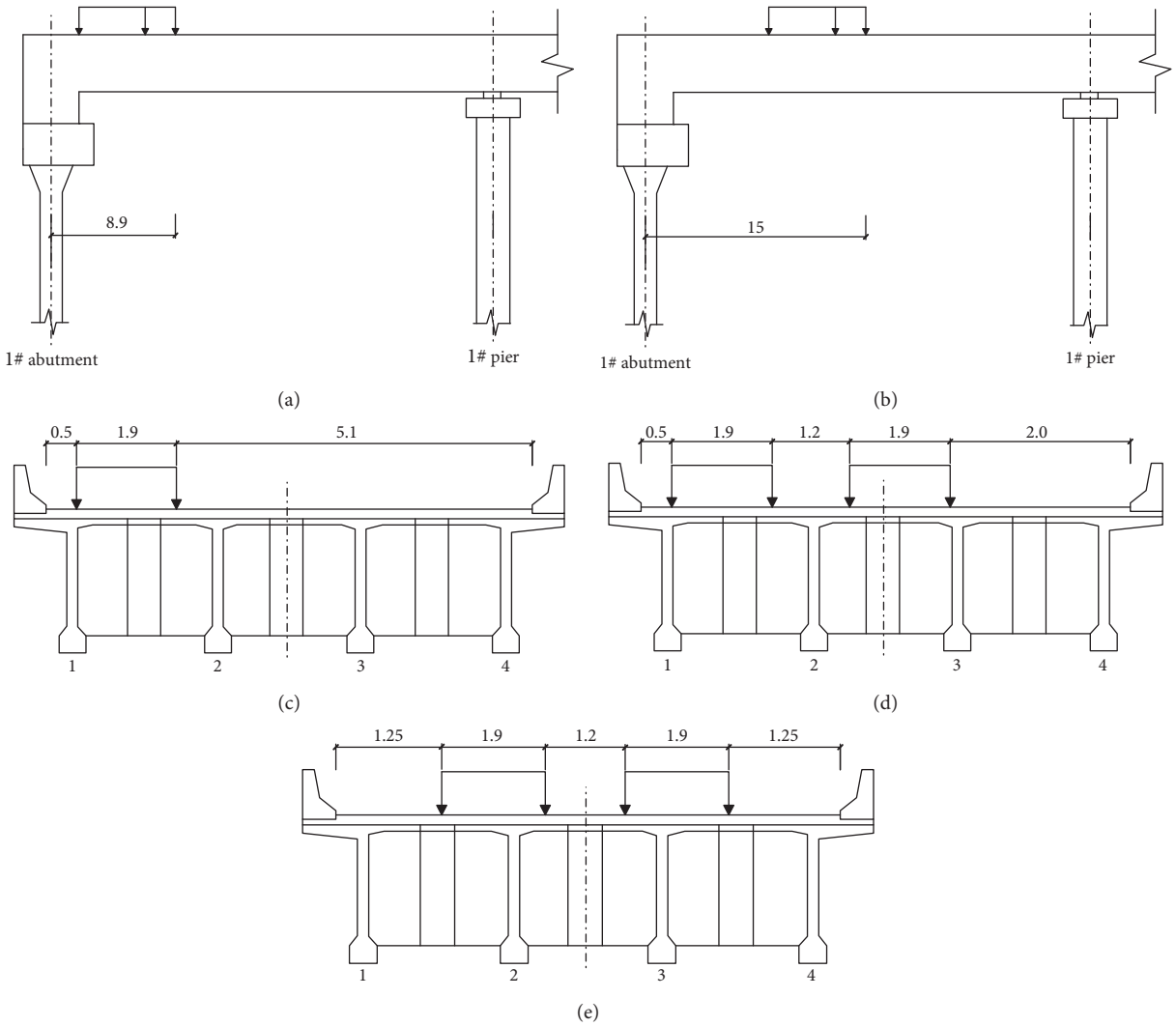

Figure 14: Load conditions (dimensions in m). (a) Longitudinal vehicle load condition I. (b) Longitudinal vehicle load condition II. (c) Transverse vehicle load condition 1. (d) Transverse vehicle load condition 2. (e) Transverse vehicle load condition 3.

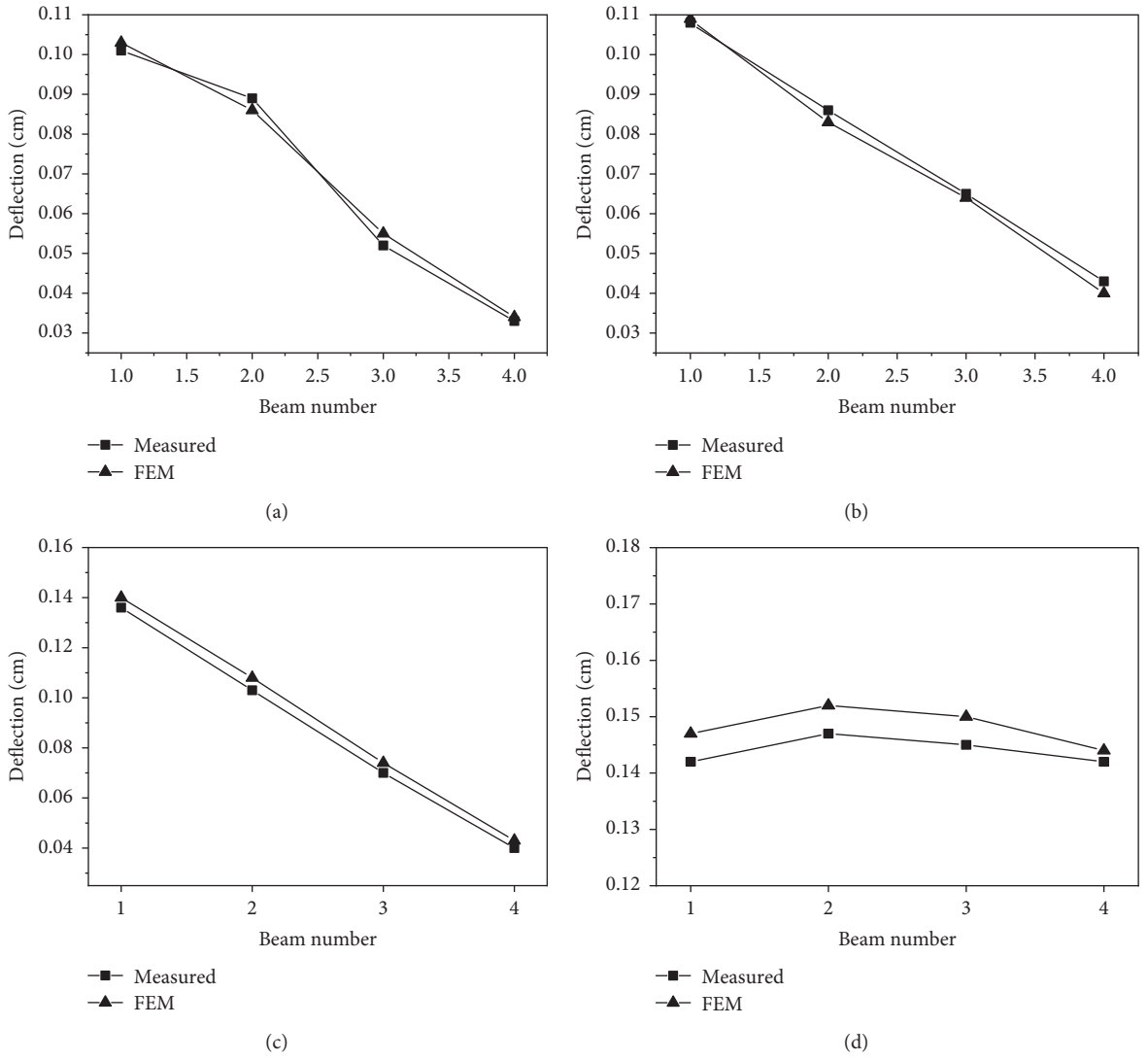

Figure 15: Comparison between numerical and experimental displacement values. (a) Deflections at section A-A during load condition I-1. (b) Deflections at section B-B during load condition I-1. (c) Deflections at section A-A during load condition II-1. (d) Deflections at section B-B during load condition I-3.

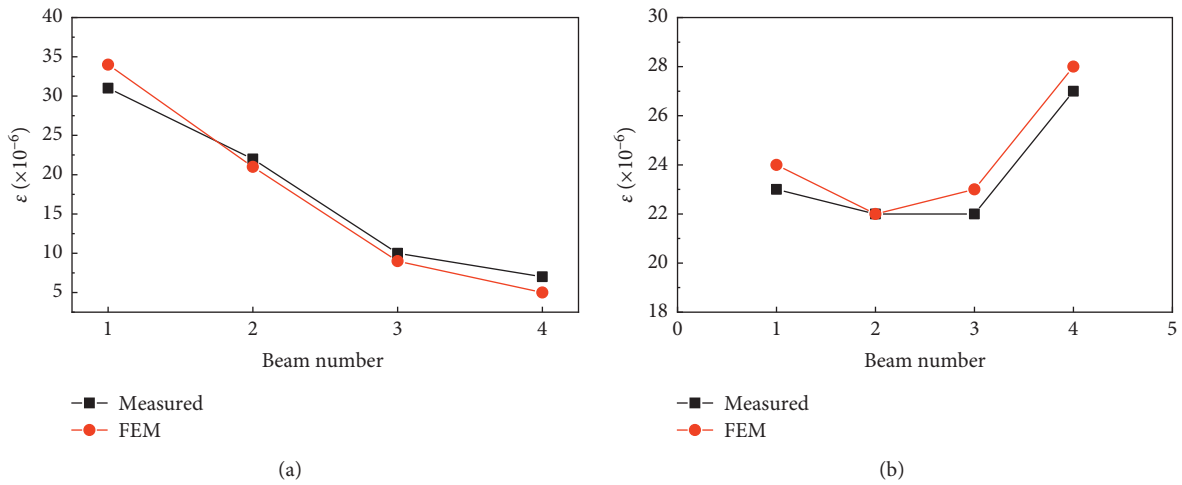

Figure 16: Continued.

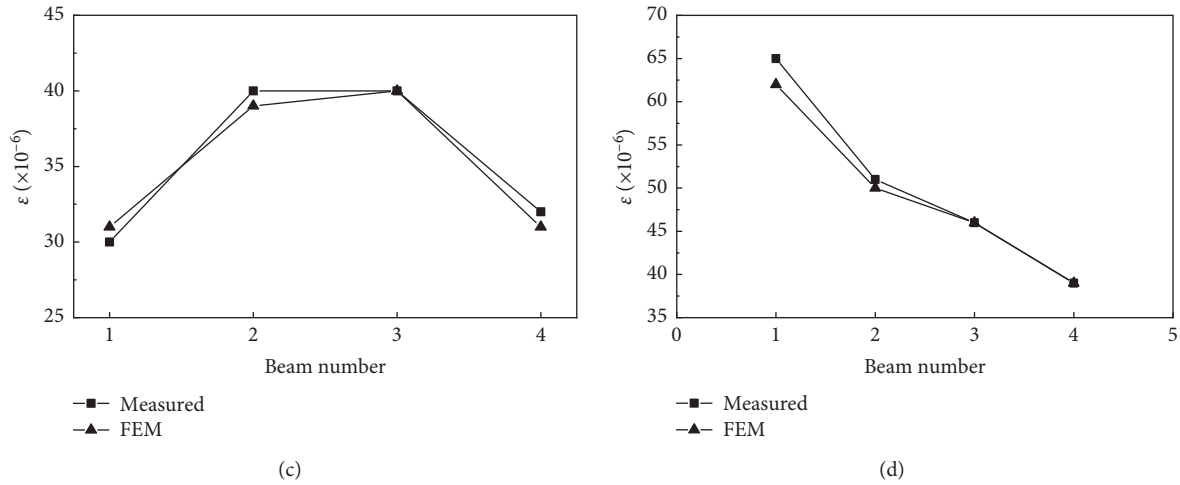

Figure 16: Comparison between numerical and experimental strain values. (a) Strain at section A-A during working condition I-1. (b) Strain at section B-B during working condition I-2. (c) Strain at section A-A during working condition I-2. (d) Strain at section B-B during working condition II-2.

order to facilitate the analysis, 12 bearings on the piers of Shangban Bridge are numbered in Figure 17.

Without the stoppers' action, the bearings' stiffness is 3,960 kN/m. The vertical force of each bearing is listed in Table 5; vertical forces of bearings are all positive, which indicates that all bearings are in compression.

(1) Bearing Antisliding Checking Calculation. It is assumed that the slipping of bearings has not occurred when the transverse displacement of bearings is 0.05 m, and the longitudinal shear force is 198 kN. According to reference ICHPD [34], the coefficient of friction between the beam and bearings is 0.3. The friction forces between bearings and beams of all piers are less than the longitudinal force of the bearings. Therefore, there is sliding between the beam and bearings before the stoppers are working.

(2) Bearing Shear Calculation. According to reference ICHPD [34], bearings have shear deflections before the stoppers are participating, and the shear deflections Δ must be constrained as

$$\Delta \leq \sum t\,[\tan\gamma],$$
$$\Delta = \frac{f\sum t}{GA}, \tag{11}$$

where t is the thickness of the rubber layer of the bearing, $[\tan\gamma]$ is the tangent value of the allowable shear angle of the bearing, f is the friction of the bearing, and G and A are the shear modulus and area of the bearing, respectively.

The vertical force of the bearings at the downstream side is the biggest vertical force. The shear deflection Δ caused by friction force is 0.062 m, which is larger than $\sum t\,[\tan\gamma] = 0.025$. This indicates that the bearings may undergo shear failure under the worst flooding. The transverse stiffness of bearings at the downstream side is 10^{10} kN/m when the stoppers are active. Then, the vertical forces of bearings of Shangban Bridge (without influence of block) are as shown in Table 6.

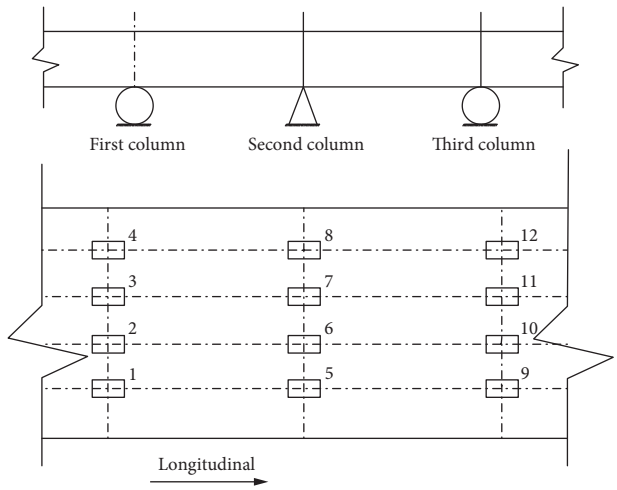

Figure 17: Arrangement of bearings.

Table 5: Vertical force of bearings of Shangban Bridge (without influence of block).

Bearing No.	Vertical force (kN)
1	183.28
2	399.63
3	495.02
4	779.25
5	186.7
6	436.56
7	491.64
8	818.77
9	183.86
10	400.1
11	493.77
12	780.31

Table 6: Vertical force of bearings of Shangban Bridge (with influence of the block).

Bearing No.	Vertical force (kN)
1	9.69
2	304.95
3	606.46
4	932.94
5	153.51
6	366.42
7	586.84
8	827.15
9	38.52
10	315.52
11	598.40
12	902.77

(3) Bearing Compressive Strength Calculation at the Downstream Side. Because of large stresses at the downstream side of bearings and large deflections under the flood force, bridge bearings may even lose their bearing capacity. According to references [3, 35, 36], bridge bearings will not lose its bearing capacity due to excessive stress or deflections under this largest flood force.

(4) Stability Calculation of Girder. From Table 6, the bearings are in compression under the largest flood force. This indicates that the overturning bending moment caused by bridge self-weight is larger than that caused by the flood force. Therefore, the girder cannot be overturned. Based on the analysis of the superstructure, under the flood force, the bearings of Shangban Bridge may have sliding and shear failure, while the vertical force of the bearings and the stability of the girder are less affected by the flood force.

5.1.2. Stress Analysis of Substructure. Piers are subjected to axial force F_z, shear force F_y, and bending moment M_x under the flood force (x represents the longitudinal direction, y represents the transverse, and z represents the vertical). Since the bottoms of piers are subjected to the biggest force, here we take the axial force F_z, shear force F_y, and bending moment M_x into account. In this section, we study only the downstream side of the piers because the shear force and bending moment at the upstream side and downstream side are very close. The arrangement of piers is shown in Figure 18.

The internal force of piers of Shangban Bridge are shown in Table 7.

According to Table 7, the axial force at the upstream side of piers under the flood force is larger than that caused by self-weight. Therefore, these piers at the upstream side are in a state of tension when the flood is coming. The axial force at the downstream side of piers under the flood force is close to that caused by self-weight. These piers at the downstream side are in a state of compression under the flood force. Meanwhile, the shear force and bending moment caused by the flood force are also much larger, so the effects on the bridge structure imposed by the flood force cannot be neglected in the bridge flood design.

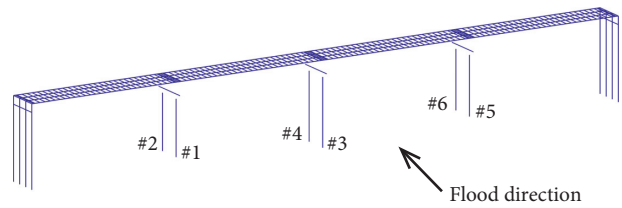

Figure 18: Arrangement of the piers.

Table 7: Internal force of the piers.

Internal force	Pier		Self-weight	Flood force
Axial force (kN)	Upstream side	1	2,567.41	−4,541.04
		3	2,580.32	−4,172.05
		5	2,608.17	−4,490.97
	Downstream side	2	2,567.40	2,602.09
		4	2,580.32	2,470.17
		6	2,608.11	2,552.63
Shear force (kN)	1		0	1,041.62
	3		0	1,139.30
	5		0	1,251.19
Moment (kN·m)	1		0	6,323.74
	3		0	6,598.40
	5		0	6,229.54

The stress of the piles can also be affected by the flood force. Since the stresses of piles of Shangban Bridge are the same, this study only takes these piles on one side into account. According to Jorgenson [37], the flood force has greater effect on those piers that lie outside the upstream and downstream side of the bridge than those that lie inside. In order to compare these results, here we take the internal forces of the cross-section at the abutment and pile joint into consideration. The internal forces of the piles both at the upstream and downstream are shown in Table 8.

The axial forces of piles caused by the flood force at the downstream side are small, while the shear force F_x and bending moment M_y caused by the flood force are very close to those caused by self-weight. From an overall perspective, the flood force can not only make the internal force of the piles increase but also much more complex. Therefore, in the bridge flood design, to calculate only the water area and wash, while neglecting the stress analysis of piers and piles under the flood force, is unreasonable.

5.2. Comparison of Four-Span Integral Abutment Jointless Bridge and Four-Span Conventional Jointed Bridge. To understand the flooding-resistant performance of the IAJB, according to ICHPD [34], Shangban Bridge can be converted into conventional jointed bridges by setting single or two-way bearings at the abutment. Bearings can be simulated by ideal springs, and the transverse constraints between the girder and abutment can be simulated by elastic connections. Then, the flooding-resistant performance of the IAJB and conventional jointed bridges is compared as follows.

Table 8: Internal force of the piles.

	Internal force	Self-weight	Flood force
Pile at upstream side	Axial force F_z (kN)	593.02	−409.86
	Shear force F_y (kN)	0	85.02
	Shear force F_x (kN)	57.71	276.67
	Moment M_y (kN·m)	80.15	471.03
	Moment M_x (kN·m)	0	85.66
Pile at downstream side	Axial force F_z (kN)	593.04	54.49
	Shear force F_y (kN)	0	85.02
	Shear force F_x (kN)	57.78	77.15
	Moment M_y (kN·m)	80.19	67.76
	Moment M_x (kN·m)	0	85.66

5.2.1. Comparison of Bearing Internal Forces. Both the internal forces of bearings at the upstream and downstream sides under self-weight and the flood force can be seen in Table 9.

From Table 9, the internal forces of the bearings of the conventional jointed bridge are larger than those of the IAJB, but their discrepancy is very small.

5.2.2. Comparison of Internal Force of Piers. Apart from the bearings, piers are also be significantly affected by the flood force, so here we takes the axial force F_z, shear force F_y, and bending moment M_x into account. Both the internal forces of piers at the upstream and downstream sides under self-weight and the flood force can be seen in Table 10.

From Table 10, as for the internal forces of the piers, the internal forces of the bearings of the conventional jointed bridge are larger than those of the integral abutment bridge (IAB), while their differences are very small.

5.2.3. Comparison of Pier Top Displacement. Based on the finite element model, here we take the maximum pier top transverse displacement of the piers into account. The maximum pier top transverse displacement of the IAJB is 2.04 cm, while that of the conventional jointed bridge is 2.07 cm. This indicates that the mechanical performance of the IAJB is very close to that of the conventional jointed bridge.

5.3. Comparison of Conventional Bridge and IAJB with Two Spans. Both Shangban Bridge and the corresponding conventional bridge are newly investigated after converting them into two-span structures.

5.3.1. Comparison of Bearing Internal Forces. Both the internal forces of the bearings in the two kinds of bridges under self-weight and the flood force can be seen in Table 11.

From Table 11, bearings at the upstream side of the IAJB are in compression, while those of the conventional jointed bridge are in tension, thus jeopardising the stability of the conventional type of structure. The results prove that both the flood-resistant and shear failure-resistant performance of IAJBs are better than those of conventional jointed bridges.

5.3.2. Comparison of Internal Forces of Piers. Comparison of internal forces of piers of the IAJB and the conventional jointed bridge can be seen in Table 12.

From Table 12, both the positive axial force of bearings of the IAJB at the downstream side and downstream side are smaller than those of the conventional jointed bridge, and the shear failure resistance of the IAJB is better than that of the conventional jointed bridge.

5.3.3. Comparison of Pier Top Displacement. Furthermore, the maximum transverse displacement of the piers is estimated, being 1.67 cm for the conventional jointed bridge and 0.55 cm for the IAJB. The results prove that the mechanical behaviour of IAJBs is better than that of the conventional jointed bridges.

6. Parametric Analysis and Comparison

The FE model of Shangban Bridge is adopted to perform parametric analyses based on variation of the following parameters: skew angle, water-blocking area, span number, pile section geometry, and abutment height. The FE structure illustrated in Figure 19 is obtained from the model described in Section 4 by converting the bearings at the abutments into sliding supports.

6.1. Skew Angle. In order to determine the influence of the skew angle on the development of passive force, Rollins and Jessee [38] performed laboratory tests on a wall with skew angles of 0°, 15°, 30°, and 45°. Pantelides et al. [39] investigated the effect of pounding for curved bridges considering soil-structure interaction effects and evaluated the effect of ground motion incidence angle on the responses of skewed bridges retrofitted with buckling-restrained braces (BRBs) in the bents. Kaviani et al. [40] proposed a detailed approach for modeling skew-angled seat-type abutments, considering a comprehensive variety of bridge configuration to identify trends in seismic behaviour of reinforced concrete bridges with seat-type abutments under earthquake loading, especially with respect to the abutment skew angle. Wang et al. [41] assessed the collapse capacity and failure modes of skewed bridges retrofitted with BRBs at the column bent, obtaining the factors controlling the seismic performance

Table 9: Reactions of bearings.

	Vertical force at downstream side (kN)	Vertical force at upstream side (kN)	Shear force (kN)
Integral abutment bridge	925.99	7.43	2,207.06
Conventional jointed bridge	1,018.45	9.95	2,229.53

Table 10: Internal force of piers.

	Axial force at downstream side (kN)	Axial force at upstream side (kN)	Shear force (kN)	Moment (kN·m)
Integral abutment bridge	5,211.37	−2,182.46	1,283.48	6,600.61
Conventional jointed bridge	5,306.43	−2,247.34	1,292.61	6,749.74

Note: negative axial force means tension and positive axial force means compression.

Table 11: Reaction of bearings.

	Axial force at downstream side (kN)	Axial force at upstream side (kN)	Shear force (kN)
Integral abutment bridge	959.49	74.38	945.98
Conventional jointed bridge	1,419.98	−104.38	1,447.86

Note: negative axial force means tension and positive axial force means compression.

Table 12: Internal force of the piers.

	Axial force at downstream side (kN)	Axial force at upstream side (kN)	Shear force (kN)	Moment (kN·m)
Integral abutment bridge	4,218.54	−972.46	583.52	4,671.75
Conventional jointed bridge	5,559.43	−1,432.13	902.88	5,367.69

Note: negative axial force means tension and positive axial force means compression.

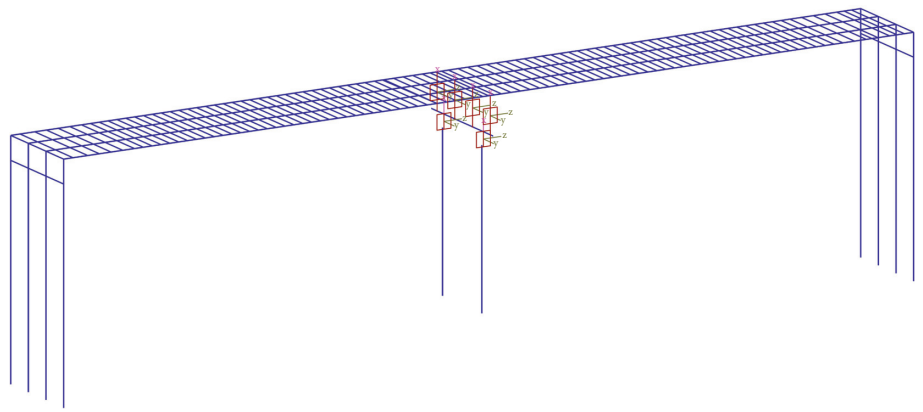

Figure 19: FEM of Shangban Bridge.

from a case study of a three-span reinforced concrete box girder skewed bridge with skew angles of 0°, 18°, 36°, and 54°.

The stiffness and strength of backfill springs linearly increase with burial depth based on the definition in Greimann and Wolde-Tinsae [9] and ICHPD [32], calculated by the "*p-y*" method considering completely elastic-plastic constitution of the soil. It is assumed that the stiffness and strength increase linearly with the angle according to Kaviani et al. [40]. In addition, the springs are always set in the normal direction of the contact surface.

The skew angle varies from 0° to 60° with increments of 15°. The parametric analysis includes the analysis of internal forces of bearings, displacement, and mechanical performance of the substructure. The results of this analysis are shown in Figure 20 (negative axial force means tension and positive axial force means compression).

From Figure 20, with the increasing skew angle, the vertical force at the downstream side and the transverse shear force of bearings and the pier and abutment top displacement increase, while the vertical forces of bearings at

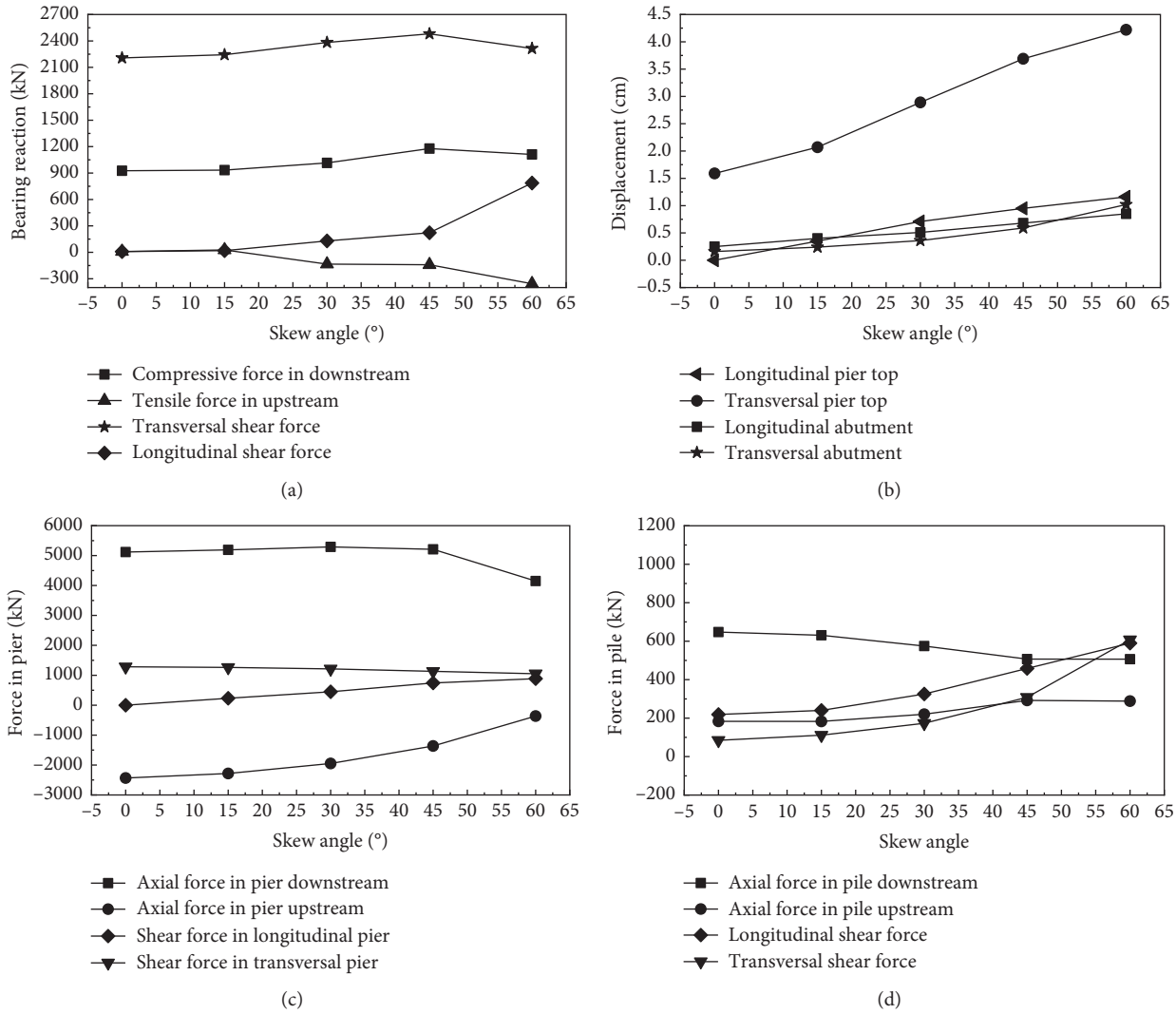

Figure 20: Variation of inner forces and deflections with skew angles. (a) Vertical force of bearings. (b) Displacement. (c) Internal force in the piers. (d) Internal force in piles.

the downstream side decrease. The transverse pier top displacement increases greatly, and the longitudinal shear force and the vertical force of piers at the upstream side increase slightly. When the skew angle is less than 45°, the vertical force of the piers at the downstream side increases slightly; while this force decreases significantly when the skew angle is greater than 45°. Meanwhile, both the longitudinal and the transverse shear force and the axial force of piles at the upstream side go up greatly, while the axial force of piles at the downstream side decreases significantly.

6.2. Water-Blocking Area. The extent of the water-blocking area exerts great influence on the action generated on the bridge. Table 13 represents the flood force per unit length connected to an increase from 1.2 m^2 to 6.0 m^2 in the water-blocking area. Figure 21 illustrates the results of the investigated mechanical parameters.

From Figure 21, with the increasing water-blocking area, the vertical force of bearings, axial force of piers, the shear force, and axial force of piles at the downstream side of bridge suffer a linear increase, while the vertical force of bearings, axial force of piers, the shear force, and axial force of piles at the upstream side of the bridge experience a linear decrease. In addition, the pier and abutment top transverse displacement also grow.

6.3. Number of Spans. Five different scenarios are studied, considering the number of spans varying from two to six. Results are displayed in Figure 22. When the number of spans is equal to or less than four, the vertical reactions of the bearings, the axial force of the piers, and the shear force and axial force of the piles located along the downstream side of bridge increase. If the number of spans exceeds four, the abovementioned quantities face a smaller variation because the abutments at the ends of the IAJB play a dominant role in the flood-resistant performance. In addition, the transverse displacements of the piers are not affected by the number of spans.

Table 13: The flood force.

Current obstruction area (m^2)	Total horizontal force (kN)	Flooding buoyancy (kN)	Wave uplift (kN)	Horizontal force in pier (kN/m)
1.2	21			
1.8	30			
3.0	50	35	21	18
4.2	69			
6.0	98			

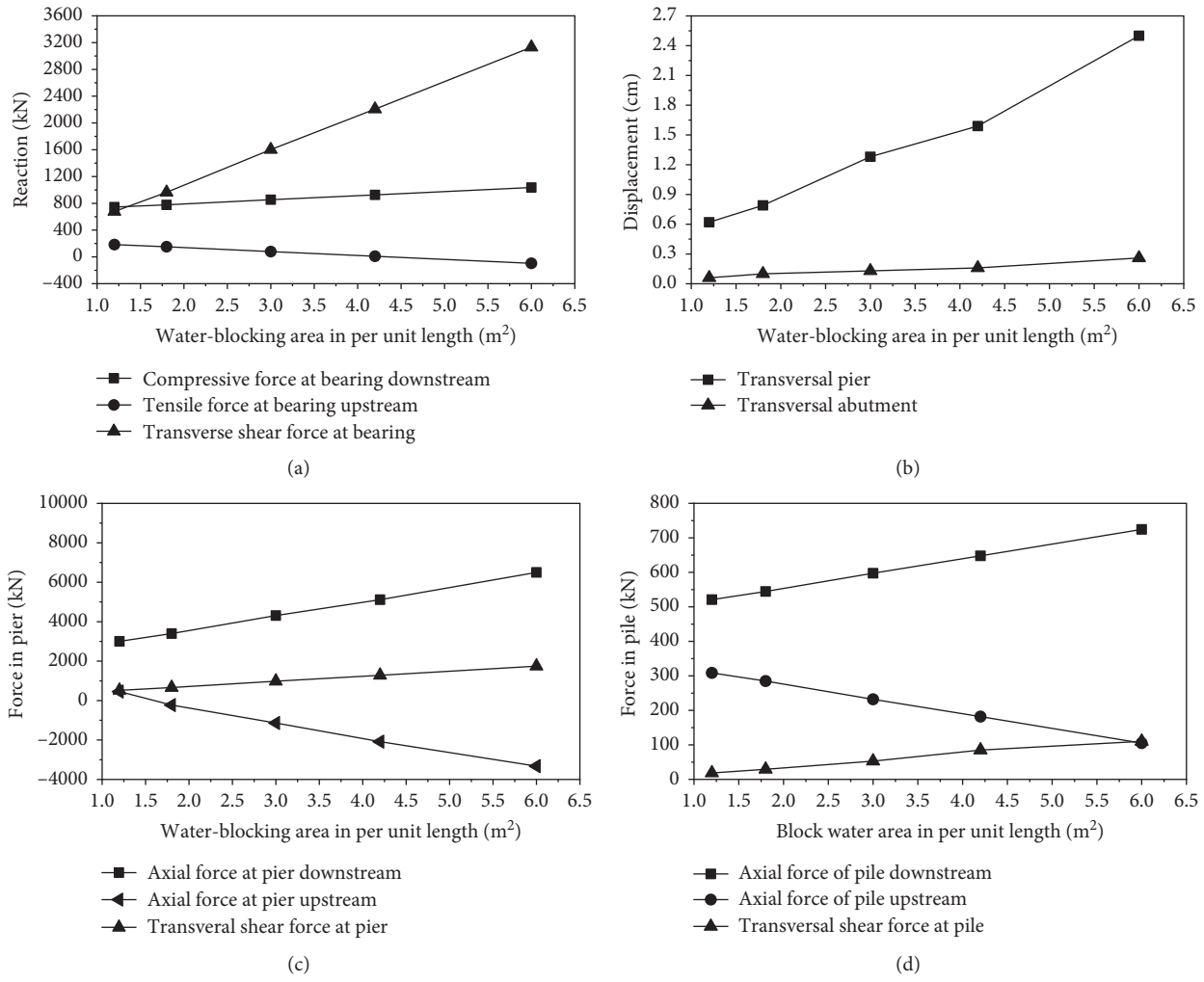

Figure 21: Variation of inner forces of structure and deflections with drag area. (a) Vertical force in bearings. (b) Displacement. (c) Internal force in piers. (d) Internal force in piles.

6.4. Pile Section Geometry. The change of the transverse pile section geometry can be represented by the relative length $\overline{B}$ [29], which is defined as

$$\overline{B} = \frac{B'}{B}, \tag{12}$$

where B and B' are the original and the modified transverse pile section geometry, respectively.

Given the transverse nature of the force exerted on the bridge by the flood, the main factors that determine the structural response are the transverse moment of inertia and the pile length. The analysis of the flooding-resistant performance of the IAJB is carried out with a relative length $\overline{B}$ ranging from 0.25 to 3.0. The results are displayed in Figure 23. The change in the pile section leads to significant variation in the generated flood force for the IAJB. As $\overline{B}$ increases, the vertical reactions of bearings and the axial and the shear forces of the piers located at the downstream side also increase.

6.5. Abutment Height. The change in the abutment height is described by the relative abutment height $\overline{H}$ [34, 42] defined as

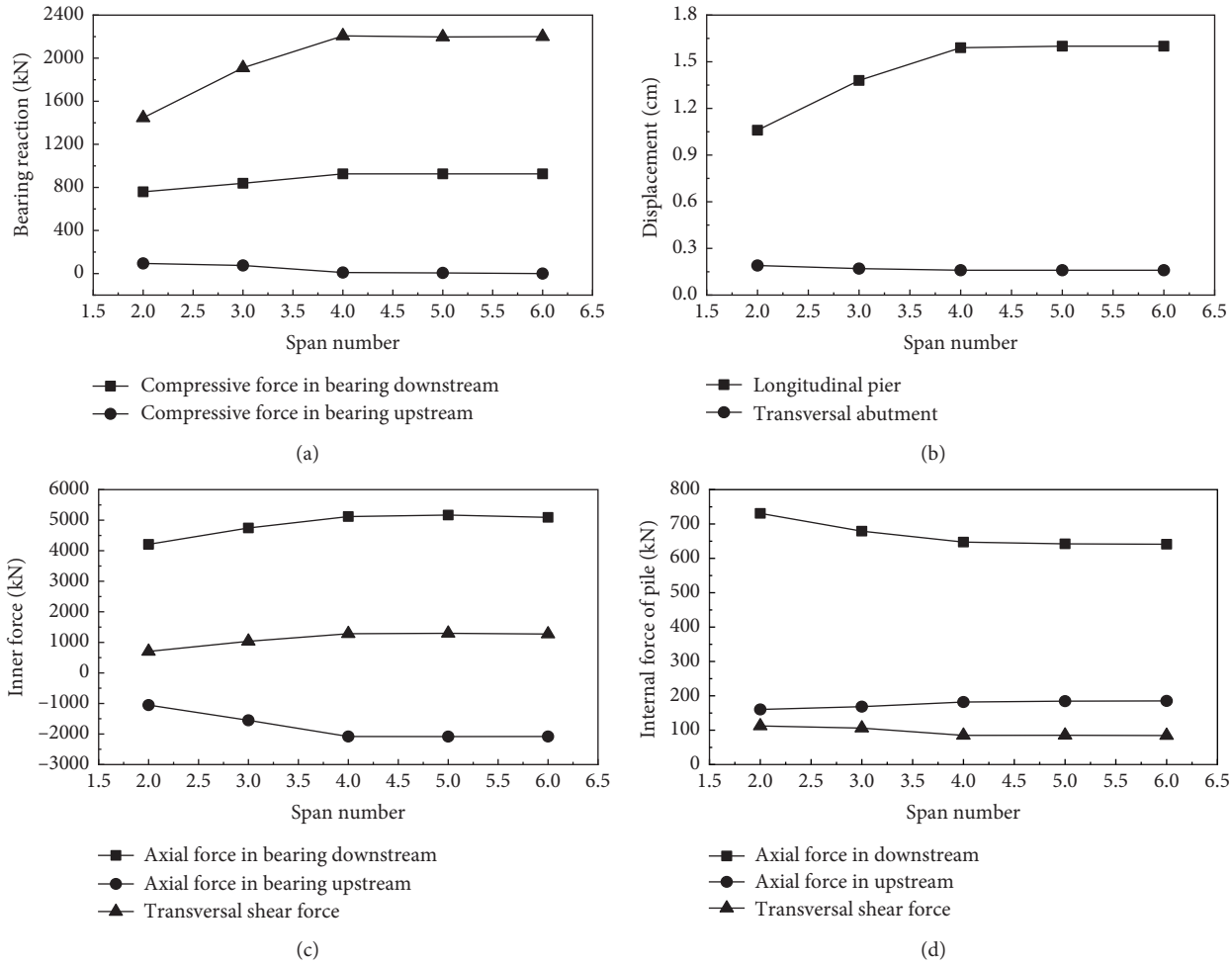

Figure 22: Variation of inner forces of structure and deflections with different numbers of spans. (a) Vertical force in bearings. (b) Displacement. (c) Internal force in piers. (d) Internal force in piles.

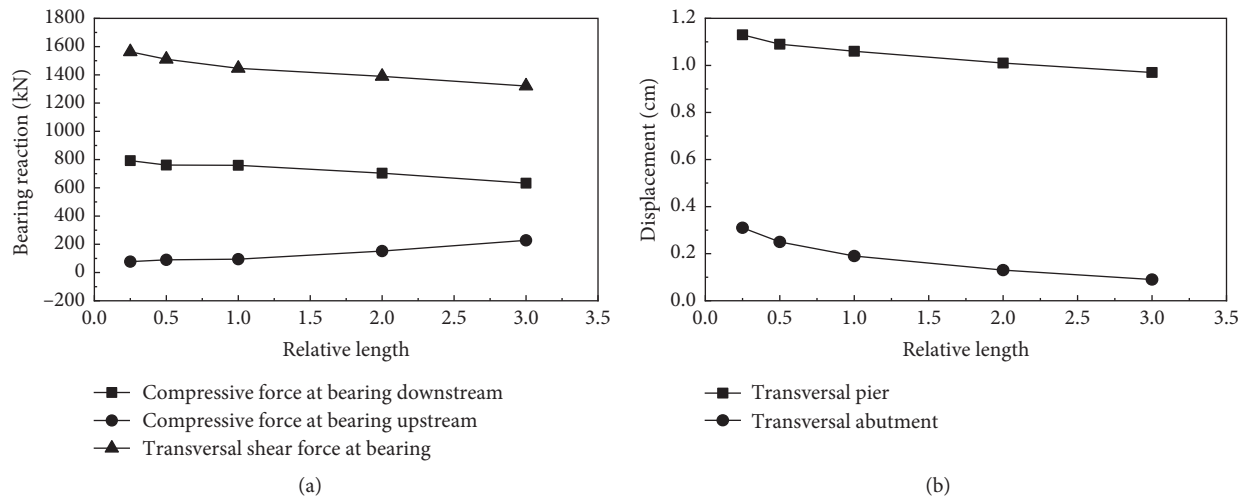

Figure 23: Continued.

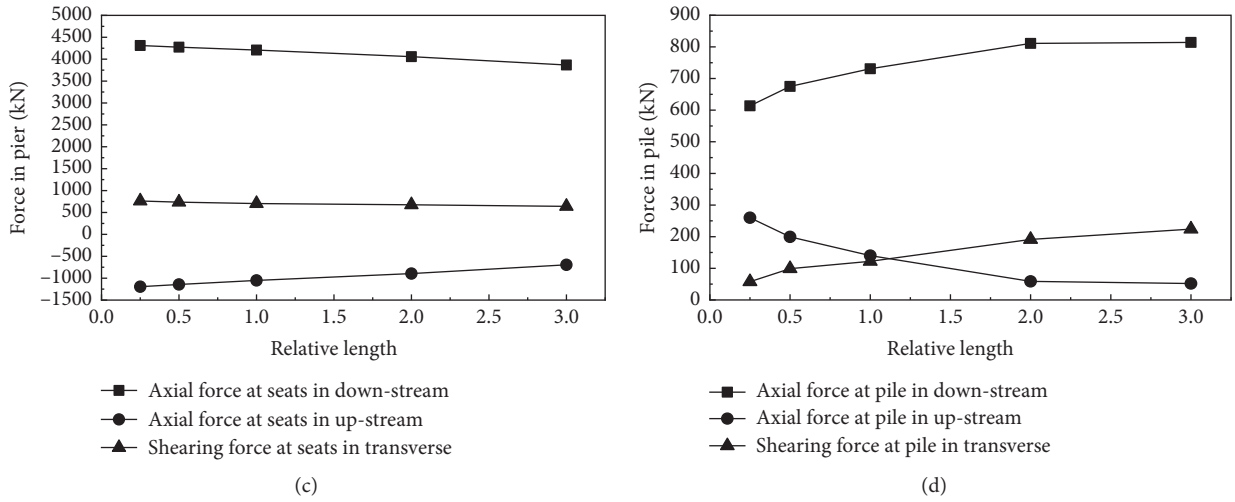

Figure 23: Variation of inner forces of structure and deflections with $\overline{B}$. (a) Vertical force in bearings. (b) Displacement. (c) Internal force in piers. (d) Internal force in piles.

$$\overline{H} = \frac{H'}{H}, \tag{13}$$

where H represents the previous abutment height and H' represents the changed abutment height.

The analysis of the flooding-resistant performance of IAJB is carried out when the relative abutment height $\overline{H}$ ranges from 0.5 to 2.5. The results connected to the change in the relative abutment height $\overline{H}$ are displayed in Figure 24. With the increase in $\overline{H}$, the vertical force of bearings, the internal force of piers and piles, and structural displacement undergo small changes, thus generating an overall limited impact on the structure.

7. Pushover Analysis

The pushover analysis investigates the dynamic response of the structure based on the equivalent plastic hinge model [43]. A static analysis, which is equivalent to a nonlinear static approach, is performed to calculate the deformation, internal force, positions, and rotation angles of the plastic hinges in the final collapse state [44]. The structure is subjected to lateral forces which are monotonically increasing until a target displacement is achieved [45].

The pushover analysis is performed using the FE model of Shangban Bridge. The position and formation sequence of plastic hinges during a flood event is examined by conducting the nonlinear static elastoplastic analysis. The lateral force loading is distributed according to an inverse triangular pattern [46, 47], and the flood loading on girders is distributed uniformly (Figure 25). The flood force increases until the value of the displacement of the middle bent cap reaches 0.5 m [48]. The values of flooding force are presented in Section 3.4.

7.1. Parameter Calculation of Stress-Strain Curves. The constitutive relationship of concrete proposed by Falamarz-Sheikhabadi et al. is adopted in this research [49–51]. Concrete grade C30 is selected, with a compressive strength of unconstrained concrete of $f'_{co} = 30$ MPa and a peak compressive strain of $\varepsilon_{co} = 0.002$. The compressive strength of concrete f'_{cc} bounded by a circular column section is [50]

$$f'_{cc} = f'_{co}\left(-1.254 + 2.254\sqrt{1 + \frac{7.94f'_1}{f'_{co}}} - 2\frac{f'_1}{f'_{co}}\right), \tag{14}$$

where f'_1 is the effective lateral confining stress and f'_{cc} is the compressive strength (peak stress) of the confined concrete:

$$f'_1 = \frac{1}{2}k_e\rho_s f_{yh}, \tag{15}$$

where k_e is the coefficient of confinement effectiveness, ρ_s is the ratio of the volume of transverse confining steel to the volume of the confined concrete core, and f_{yh} is the yield strength of the transverse reinforcement. For spiral bars, the coefficient of confinement effectiveness is

$$k_e = \frac{A_e}{A_{cc}} = \frac{\pi/4d^2\left(1 - \left(s'/2d_s\right)\right)^2}{\pi/4d^2\left(1 - \rho_{cc}\right)} = \frac{\left(1 - \left(s'/2d_s\right)\right)^2}{1 - \rho_{cc}}, \tag{16}$$

where s' is the vertical spacing between spiral or hoop bars, d_s is the diameter of spiral between bar centers, ρ_{cc} is the ratio of area of longitudinal reinforcement to area of core of section, A_e is the area of effectively confined concrete core, A_{cc} is the area of core of section enclosed by the centerlines of the perimeter spiral or hoop, and ρ_s is a parameter expressed as

$$\rho_s = \frac{4A_{sp}}{d_s s}, \tag{17}$$

where A_{sp} is the area of transverse reinforcement bar and s is the center-to-center spacing or pitch of a spiral or circular hoop. The compressive strain ε_{cc} corresponding to f'_{cc} is

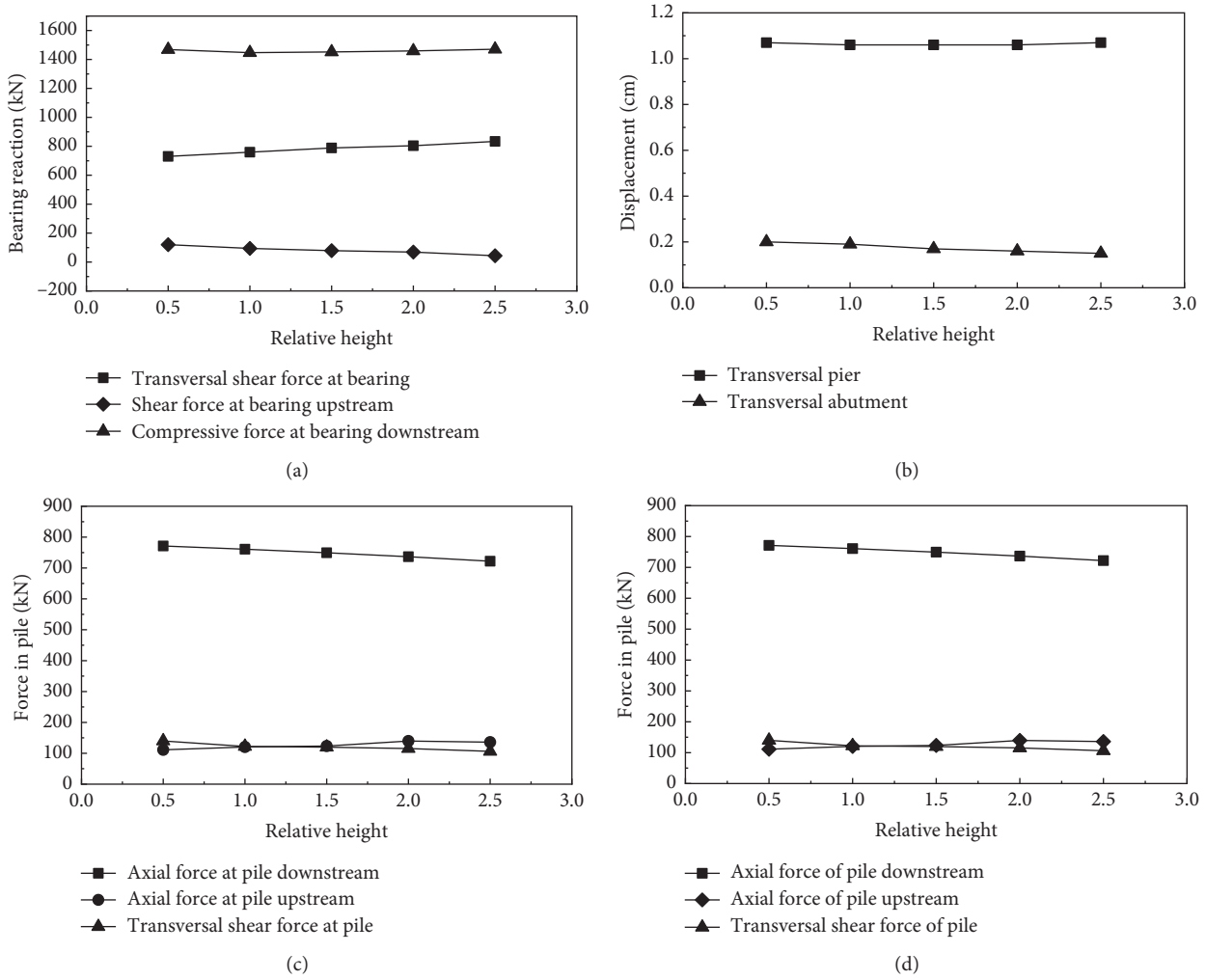

FIGURE 24: Variation of inner forces of structure and deflections with $\overline{H}$. (a) Vertical force in seats. (b) Displacement. (c) Inner force in piers. (d) Inner force in piles.

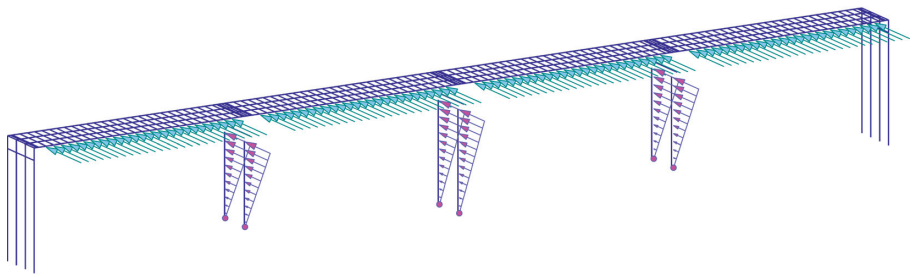

FIGURE 25: Sketch of loading distribution in pushover analysis.

$$\varepsilon_{cc} = \varepsilon_{c0}\left(1 + 5\left(\frac{f'_{cc}}{f'_{co}} - 1\right)\right). \tag{18}$$

The constraint effective coefficient of a rectangular confined concrete section is

$$k_e = \frac{\left(1 - \sum_{i=1}^{n}\left((w'_i)^2/6b_c d_c\right)\right)\left(1 - (s'/2d_c)\right)}{1 - \rho_{cc}}, \tag{19}$$

where b_c and d_c are the core dimensions to centerlines of the perimeter hoop in the x and y directions, respectively, where

Table 14: Parameters related to confined concrete strength.

	A_e (mm^2)	A_{cc} (mm^2)	k_e	F_{yh} (N/mm^2)	A_{sp} (mm^2)	f_1' (N/mm^2)	f_{cc}' (N/mm^2)	ε_{cc}
Section of column	1.391	1.590	0.875	235	28.3	0.041	30.275	0.0021
Section of pile	0.148	0.279	0.530	235	A_{sx} 56.6 A_{sy} 56.6	f_{lx}' 0.055 f_{ly}' 0.080	30.435	0.0022

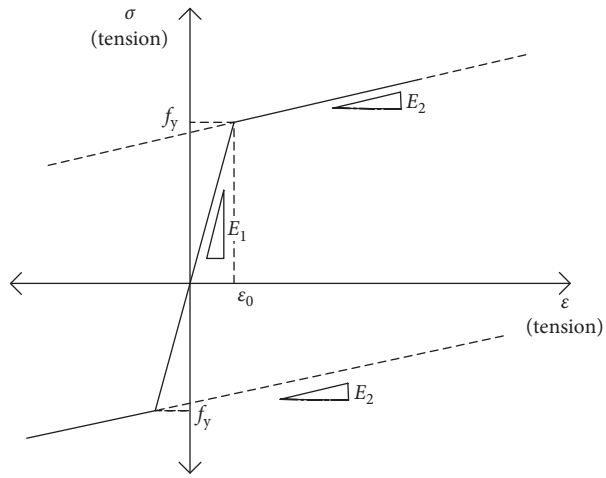

Figure 26: Stress-strain curve of reinforcement.

Table 15: Cracking, yield, and ultimate strengths and corresponding curvature values of piles 1–4.

	Cracking strength (kN·m)	Cracking curvature (1/m)	Yield strength (kN·m)	Yield curvature (1/m)	Ultimate strength (kN·m)	Ultimate curvature (1/m)
Pile 1	446.082	$3.640E-03$	584.829	$5.694E-02$	438.160	0.12582
Pile 2	445.693	$3.632E-03$	584.707	$5.697E-02$	438.118	0.12583
Pile 3	445.307	$3.623E-03$	584.585	$5.701E-02$	438.075	0.12585
Pile 4	444.922	$3.615E-03$	584.462	$5.704E-02$	438.033	0.12587

Table 16: Cracking, yield, and ultimate strengths and corresponding curvature values of piles 5–8.

	Cracking strength (kN·m)	Cracking curvature (1/m)	Yield strength (kN·m)	Yield curvature (1/m)	Ultimate strength (kN·m)	Ultimate curvature (1/m)
Pile 5	445.839	$3.635E-03$	584.753	$5.697E-02$	438.134	0.12583
Pile 6	445.588	$3.629E-03$	584.674	$5.699E-02$	438.106	0.12584
Pile 7	445.336	$3.624E-03$	584.594	$5.701E-02$	438.075	0.12585
Pile 8	445.083	$3.618E-03$	584.513	$5.703E-02$	438.051	0.12586

$b_c > d_c$, and w_i' is the i^{th} clear distance between adjacent longitudinal bars. Transverse confining steel in the x and y directions may be expressed as

$$r_x = \frac{A_{sx}}{sd_c},$$
$$r_y = \frac{A_{sy}}{sb_c}, \tag{20}$$

where A_{sx} and A_{sy} are the total areas of transverse bars along the x and y directions, respectively. The effective constraint stresses, f_{lx}' and f_{ly}' along the x and y directions are calculated as

$$f_{lx}' = k_e r_x f_{yh},$$
$$f_{ly}' = k_e r_y f_{yh}. \tag{21}$$

The lateral confining stress strength of the rectangular section is determined by the largest confining stress ratio f_{12}'/f_{co}' and the smallest confining stress ratio f_{11}'/f_{co}'. Table 14 displays the relevant parameters required to determine the peak compressive strength and compressive strain of the concrete.

Table 17: Cracking, yield, and ultimate strengths and corresponding curvature values of columns 1–6.

	Cracking strength (kN·m)	Cracking curvature 1/m)	Yield strength (kN·m)	Yield curvature (1/m)	Ultimate strength (kN·m)	Ultimate curvature (1/m)
Column 1	1,826.400	$3.746E-04$	3 568.970	$1.399E-02$	3,466.431	$7.272E-02$
Column 2	1,830.614	$3.757E-04$	3 573.003	$1.397E-02$	3,467.269	$7.262E-02$
Column 3	2,034.438	$7.447E-04$	3 524.484	$1.427E-02$	3,444.233	$7.360E-02$
Column 4	2,026.090	$7.376E-04$	3 536.525	$1.420E-02$	3,443.405	$7.362E-02$
Column 5	1,830.493	$3.756E-04$	3 587.407	$1.388E-02$	3,470.274	$7.229E-02$
Column 6	1,832.188	$3.760E-04$	3 589.235	$1.386E-02$	3,470.106	$7.204E-02$

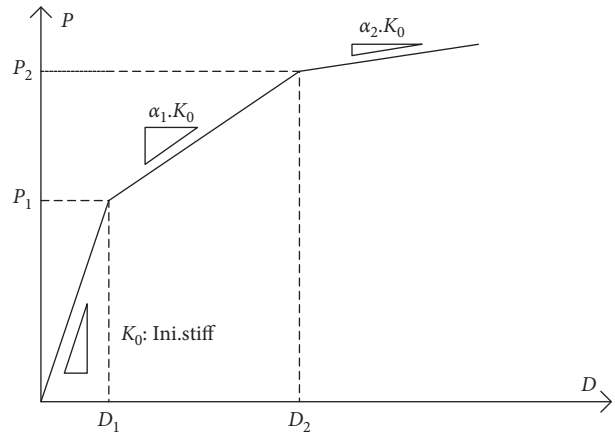

Figure 27: Three-fold line model of moment-curvature constitutive relationship.

Table 18: Stiffness and reduction factor of rectangular piles.

	Pile 1	Pile 2	Pile 3	Pile 4	Pile 5	Pile 6	Pile 7	Pile 8
K_0 (kN·m^2)	122,528	122,710	122,892	123,075	122,642	122,760	122,879	122,998
α_1 $(E-02)$	2.1244	2.1236	2.1229	2.1221	2.1239	2.1234	2.1229	2.1224
A_2	0							

Table 19: Stiffness and reduction factor of columns.

	Column 1	Column 2	Column 3	Column 4	Column 5	Column 6
K_0 (kN·m^2)	4,874,860	4,872,320	2,731,580	2,746,810	4,872,800	4,871,290
α_1 $(E-02)$	2.6243	2.6305	4.0310	4.0832	2.6702	2.6733
α_2	0					

The stress-strain curve of the steel bar is defined according to the symmetrical model, as shown in Figure 26. The steel bar is HPB235 (equivalent to BST420S in Germany) [24]; its yield strength is 235 MPa, $E_1 = 200$ GPa, and the stiffness reduction factor E_2/E_1 is 0.01.

7.2. Moment-Curvature Curve. The Shangban Bridge has a total of 4×2 rectangular piles under the abutment and 6 columns. Theoretical moment-curvature relationships for reinforced concrete-column sections can be calculated using well-known theory [52], which assumes that plane sections before bending remain plane after bending. Considering the axial force obtained by static analysis, we used the stress-strain relations for confined and unconfined concrete developed by Mander et al. and the two-fold line stress-strain model for steel to obtain the moment-curvature relations of the piers and piles. Their cracking strength, yield strength, and ultimate strength are listed in Tables 15–17. The ultimate curvature is used to determine the first part of the structure where plastic hinges appear [53].

The characteristic value of the plastic hinge is defined by the three-fold line model (as shown in Figure 27). The initial stiffness K_0, the second stiffness K_1, and the third stiffness K_2 are obtained according to the M-φ calculations. Therefore, the stiffness reduction factors α_1 and α_2 can be estimated, as reported in Tables 18 and 19.

7.3. Pushover Results. The pushover analysis is conducted by applying flooding force with an inverted triangular pattern on both Shangban Bridge and conventional jointed bridge.

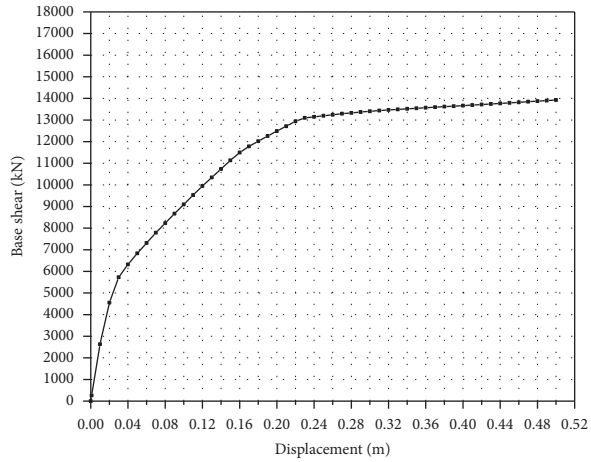

Figure 28: Base shear force-displacement curve of IAJB.

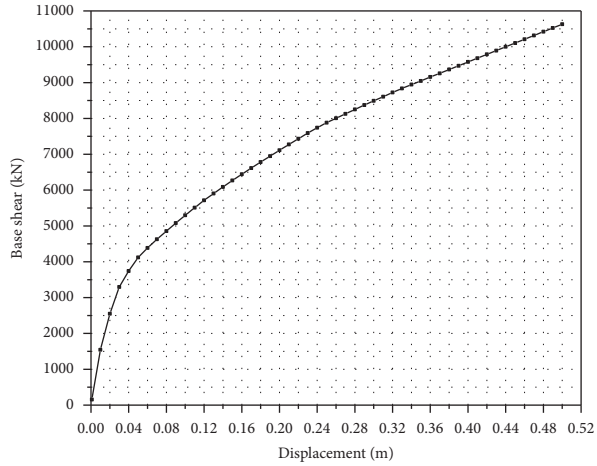

Figure 29: Base shear force-displacement curve of the conventional jointed bridge.

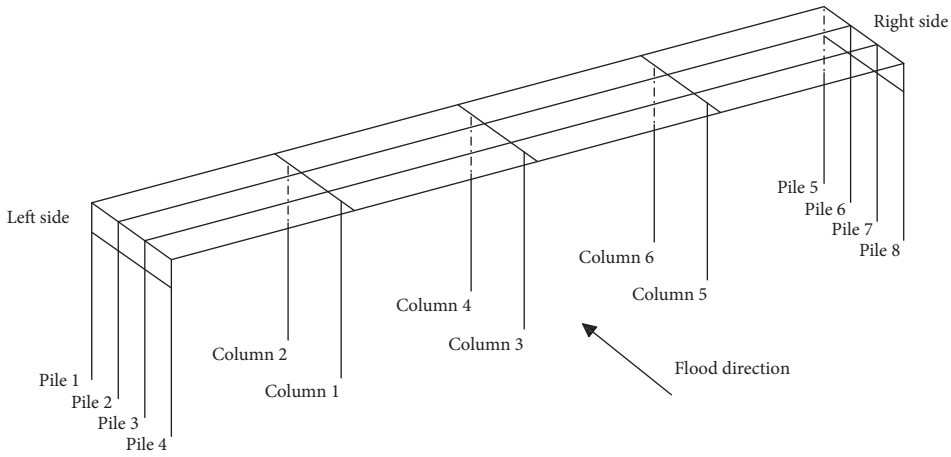

Figure 30: Simplified structure of Shangban Bridge.

Figures 28 and 29 display the shear force, displacement curves showing the base shears of piers corresponding to the displacement at the top of the middle bent cap. Firstly, we exported the results of the software analysis (deformation of key points of the pile and column). Then, we found the analysis step where the curvature exceeds the limit curvature of the section for the first time. From the text data of the pushover figure we found the displacement (called maximum allowable displacement hereafter) of IAJB and conventional jointed bridge when first plastic hinge occurs,

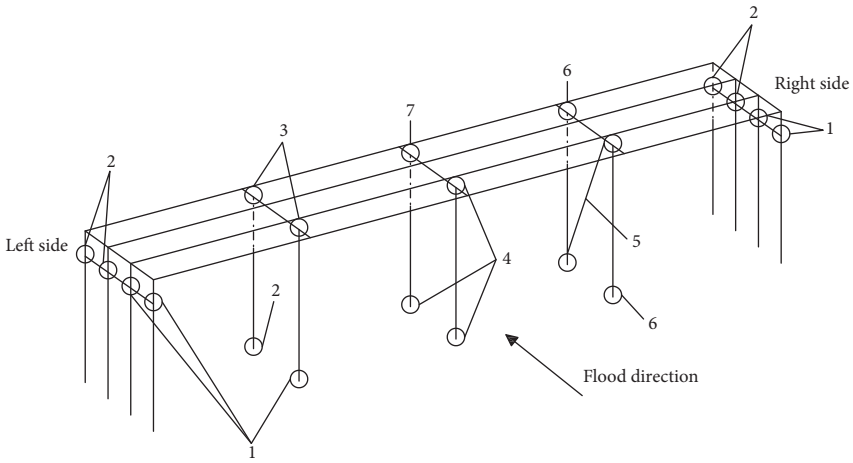

Figure 31: The order of occurrence of plastic hinges.

Table 20: Base shears at piers corresponding to occurrence sequence of plastic hinges.

Step	Base shear (kN)	Remark
1	11,825~12,067	Plastic hinges first appear in piles 3, 4, 7, 8, and then at the bottom of column 1
2	12,308~12,538	Plastic hinges occur in piles 1, 2, 5, 6 and at the bottom of column 2
3	12,993~13,109	Plastic hinges appear at the top of column 1 and 2
4	13,342~13,503	Plastic hinges develop at the bottom of column 4 and at the top and bottom of column 3
5	13,528~13,552	Plastic hinge forms at the bottom of column 5 and then develops at the top of column 5
6	13,566~13,743	Plastic hinge forms at the bottom of column 6 and then develops at the top of column 6
7	13,788~13,831	The last plastic hinge appears at the top of column 4

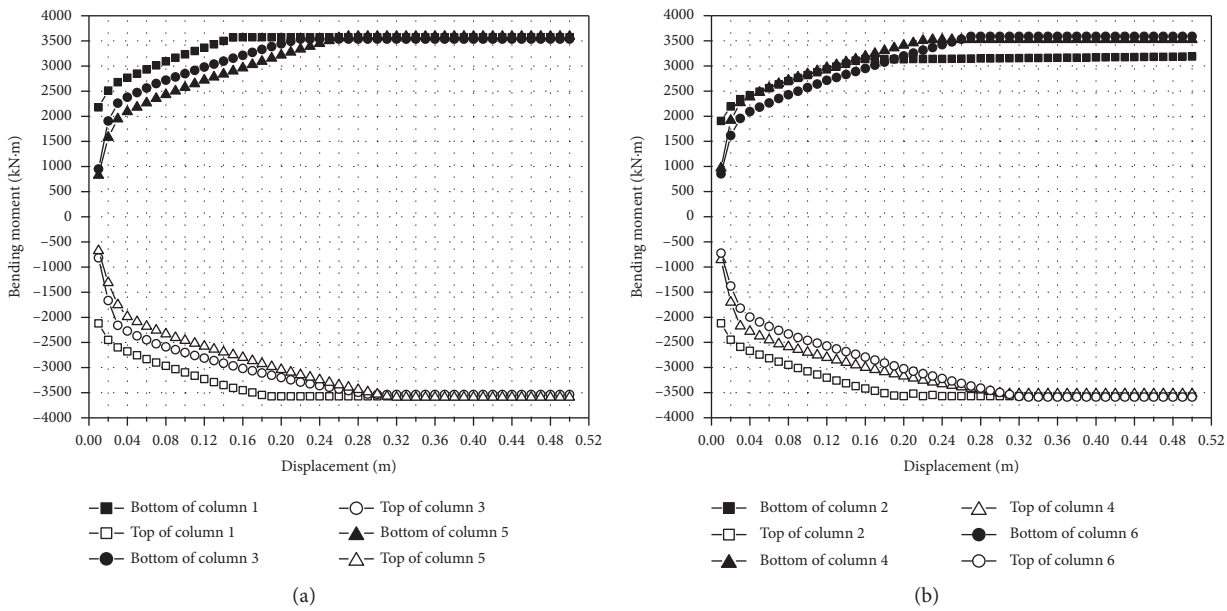

Figure 32: Moment-displacement at the top and bottom of the piers. (a) Moment-displacement at the top and bottom of the piers at the upstream side. (b) Moment-displacement at the top and the bottom of the piers at the downstream side.

which were 0.17 m and 0.138 m, respectively, in the corresponding step. The first knuckle point in may be caused by geometric nonlinearity and not nonlinearity induced by occurrence of the first plastic hinge. Besides, it is found out that the lateral ultimate bearing capacity is 11,825 kN and 6,251 kN, respectively.

In order to display the plastic hinges conveniently, the Shangban Bridge model is represented by a simplified frame structure in Figures 30 and 31. The occurrence sequence of plastic hinges is depicted in Figure 31. Base shears at the piers corresponding to the occurrence sequence of plastic hinges is listed in Table 20.

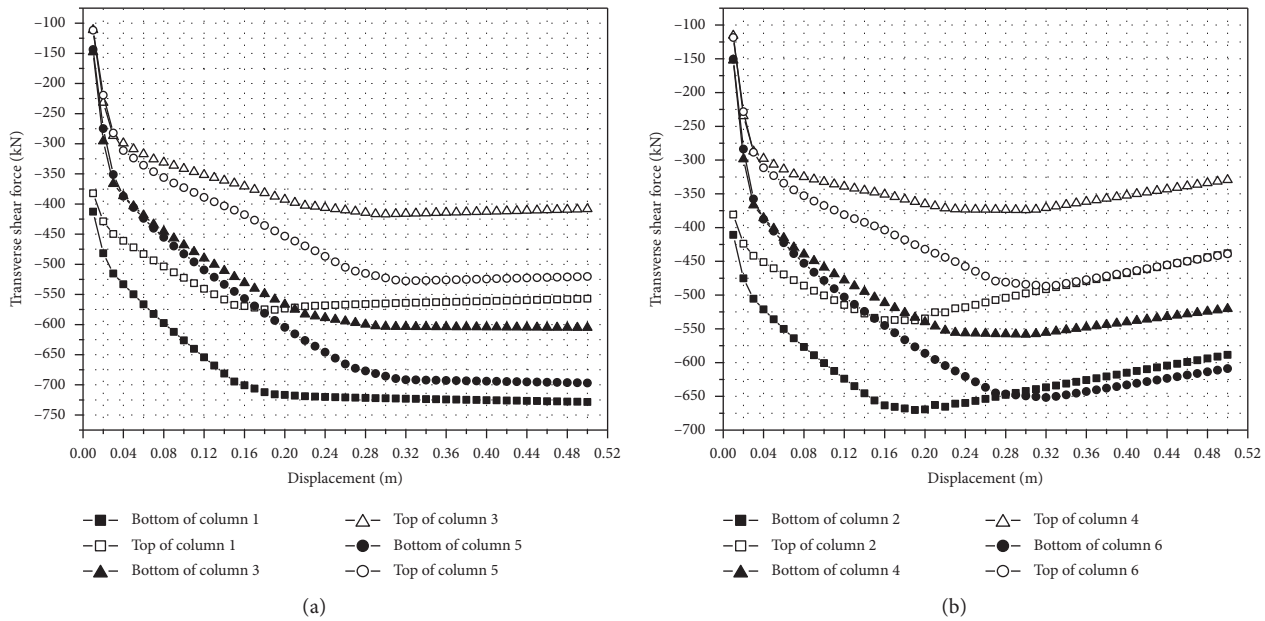

Figure 33: Transverse shear force-displacement at the top and bottom of the piers. (a) Transverse shear force-displacement at the top and bottom of the piers at the upstream side. (b) Transverse shear force-displacement at the top and bottom of the piers at the downstream side.

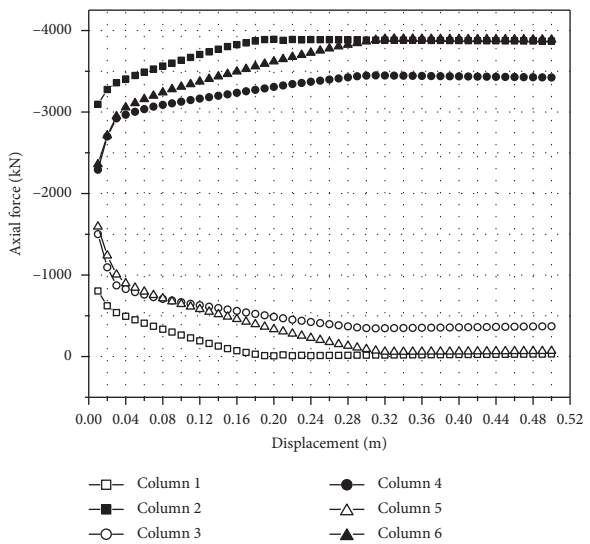

Figure 34: Axial force-displacement at the bottom of the bridge pier.

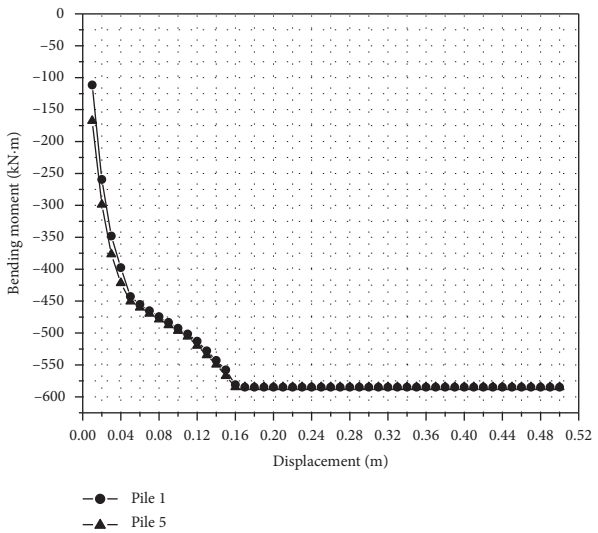

Figure 35: Moment-displacement at the top of typical piles.

It can be seen from Table 20 that the plastic hinges first occur at the top of piles 3, 4, 7, and 8 and then appear at the bottom of column 1 when the base shear is within 11,825 kN~12,067 kN. When base shear reaches 12,308 kN to 12,538 kN, the plastic hinges occur in piles 1, 2, 5, 6, and at the bottom of column 2. Plastic hinges develop at the top of columns 1 and 2 when base shear reaches 12,993 kN to 13,109 kN. When the flooding force goes up, a further plastic hinge appears in sequence at the bottom of column 4, then at the top and bottom of column 3, then at the bottom of column 5, and finally at the top of column 5. When base shear reaches 13,566 kN to 13,743 kN, plastic hinges occur at the top and bottom of column 6, and finally develop at the top of column 4.

The development of the bending moment at the upstream and downstream sides of the top and bottom of piers, respectively, is depicted in Figure 32. It is shown that the bending moment at the top and bottom of the columns increases until plastic failure occurs and that the bending moment finally stabilises about the absolute value of 3,500 kN·m. Besides with the appearance of the plastic hinge, the bending moment at the pier top appears a little bit larger than that of the pier bottom.

The development of transverse shear force at the upstream and downstream sides of the top and bottom of piers is portrayed in Figure 33. Initially, we can see that the shear

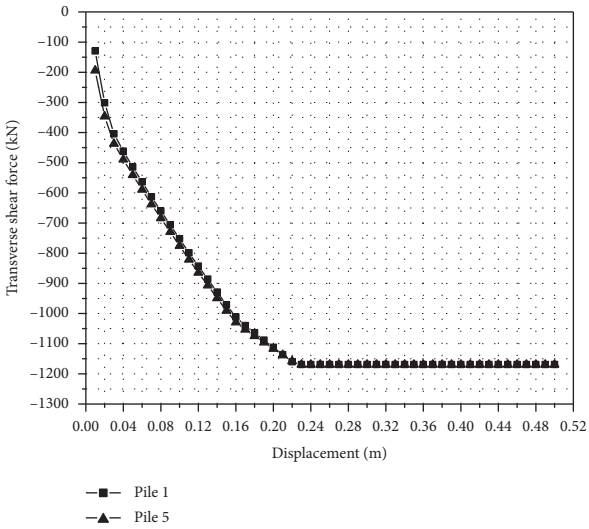

Figure 36: Transverse shear force-displacement at the top of typical piles.

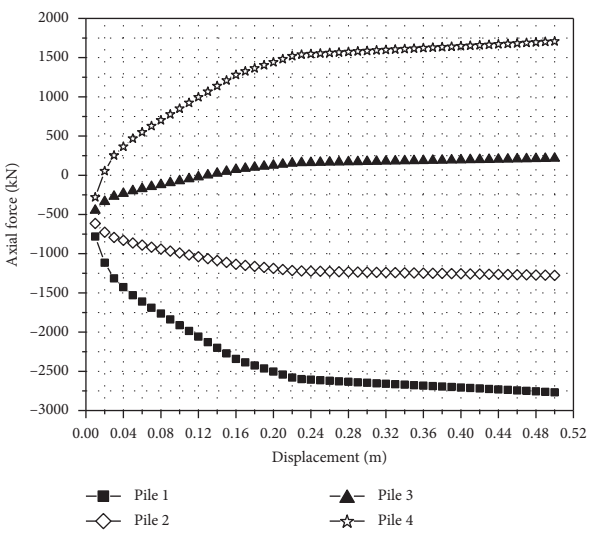

Figure 37: Axial force-displacement at the top of piles 1–4.

force of the piers along the upstream side increases, and afterwards it tends to stabilise. However, the shear force of the piers along the downstream side tends to decrease when plastic hinges occur. In addition, the shear force at the bottom of the piers is larger than that at the top of the piers. In comparison, the shear force of piers at the upstream side is approximately 50–100 kN larger than that at the downstream side.

The development of the axial force of the piers is described in Figure 34. It can be seen that the axial force of the columns at the downstream side increases and finally stabilises at approximately −4,000 kN. Due to flooding force, the piers at the upstream side tend to be lifted up, causing the gradual decrease in the value of the axial force. The axial forces of column 1 and column 3 are the smallest, approximately equal to zero.

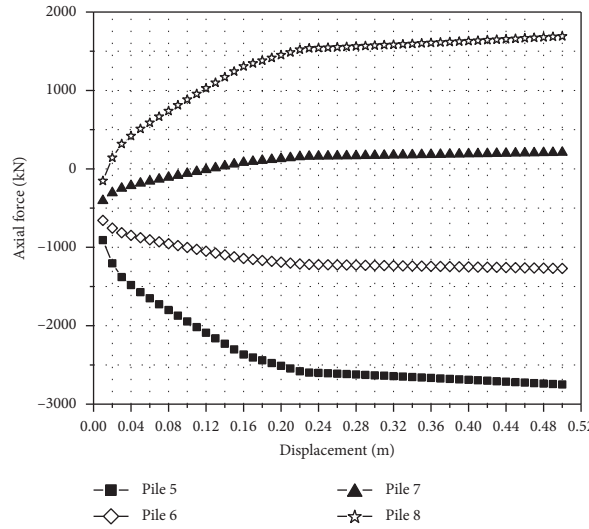

Figure 38: Axial force-displacement at the top of piles 5–8.

All the piles perform in the same fashion, therefore, only the inner force of pile 1 at the left side abutment and pile 5 at the right side abutment are provided. Figure 35 depicts the bending moment-displacement relationship, Figure 36 shows transverse shear force-displacement at the top of typical piles, and Figures 37 and 38 display the axial force-displacement relationship. Due to the action of the flood, the piers at the upstream side tend to be lifted up, which leads to a gradual decrease in the axial forces. The axial force along the downstream side gradually increases, while the state of the piles along the upstream side changes from compression to tension. Both the bending moment and the shear force in the piles increase and finally reach stable values at approximately 600 kN·m and 1,200 kN, respectively.

The maximum displacements of the IAJB and the conventional jointed bridge are 0.17 m and 0.138 m, respectively, while their lateral ultimate bearing capacities are 11,825 kN and 6,251 kN, respectively. It can be seen that the maximum transverse displacement of the IAJB is larger than that of the conventional jointed bridge by 23.2 percent and that the maximum lateral ultimate bearing capacity of the IAJB is larger than that of the conventional jointed bridge by 89.2 percent. Then, a vital conclusion can be made so that the IAJB has better flooding-resistance performance than the conventional jointed bridge.

8. Conclusion

Parametric investigation on flooding-resistant performance of an integral abutment and jointless bridge was conducted via the finite element method (FEM) in this paper. Firstly, a corresponding numerical model was created and validated based on a field test. Secondly, dozens of parametric analyses were carried out to assess the effects of parameters such as skew angle, water-blocking area, span number, pile section geometry, and abutment height on flood-resistant performance of the IAJB. Finally, a pushover analysis was conducted to reveal

the ultimate state of the IAJB under flooding force through the estimation of maximum transverse displacement and the occurrence sequence of plastic hinges on the whole IAJB's structure. Corresponding conclusions can be made as follows:

(1) The flooding-resistant performance of IAJBs is better than that of conventional continuous jointed bridges only when the number of spans is less than 4.

(2) The flood-resistant performance of IAJBs is significantly affected by skew angle, water-blocking area, and pile section geometry, but little affected by abutment height. In particular, the larger the skew angle is, the higher the protection on seats will be. However, this does not mean that only a large deflection angle can improve the flood-resistant performance of the whole bridge; other parameters need to be considered comprehensively. In addition, the flood-resistant performance of IAJBs improves with the decrease of the water-blocking area.

(3) Plastic hinges in the IAJB first appeared in the pier foundation near the left abutment upstream and the pile body below the left abutment upstream. With increase of the flooding force, plastic hinges will develop at the downstream side of pile top and pier bottom that close to left abutment and then will develop to other side of the bridge in longitudinal direction. Finally, plastic hinge was developed at the middle pier top on the downstream side.

(4) The IAJ Bridge is apparently better in flooding-resistance performance than the conventional bridge with higher allowable bearing force and allowable transverse displacement.

Data Availability

The data used to support the findings of this study are available from the corresponding author upon request.

Conflicts of Interest

The authors declare that they have no conflicts of interest.

Acknowledgments

The authors appreciate the support from the Natural Science Foundation of China through no. 51778147 as well as the Zhejiang Provincial Natural Science Fund (no. LY17E080022).

References

[1] B. Ghorbani, "A field study of scour at bridge piers in flood plain rivers," *Turkish Journal of Engineering and Environmental Sciences*, vol. 32, no. 4, pp. 189–199, 2008.

[2] Q. Zhao, C. Lin, Y. Zhao, and G. Huang, "Mechanical characteristics of a new type of jointless bridge with an arch structure," in *Proceedings of the 2018 3rd International Conference on Smart City and Systems Engineering (ICSCSE)*, pp. 300–307, IEEE, Xiamen, China, December 2018.

[3] I. Husain and D. Bagnariol, "Design and performance of jointless bridges in ontario: new technical and material concepts," *Transportation Research Record: Journal of the Transportation Research Board*, vol. 1696, no. 1, pp. 109–121, 2000.

[4] D. M. Barbieri, Y. Chen, E. Mazzarolo, B. Briseghella, and A. M. Tarantino, "Longitudinal joint performance of a concrete hollow core slab bridge," *Transportation Research Record: Journal of the Transportation Research Board*, vol. 2672, no. 41, pp. 196–206, 2018.

[5] J. Witzany and T. Cejka, "Reliability and failure resistance of the stone bridge structure of Charles Bridge during floods," *Journal of Civil Engineering and Management*, vol. 13, no. 3, pp. 227–236, 2007.

[6] Y.-Y. Ko, J.-S. Chiou, Y.-C. Tsai, C.-H. Chen, H. Wang, and C.-Y. Wang, "Evaluation of flood-resistant capacity of scoured bridges," *Journal of Performance of Constructed Facilities*, vol. 28, no. 1, pp. 61–75, 2014.

[7] I. Qeshta, *Fragility and Resilience of Bridges Subjected to Extreme Wave-Induced Forces*, RMIT University, Melbourne, Australia, 2019.

[8] D. D. Girton, T. R. Hawkinson, and L. F. Greimann, "Validation of design recommendations for integral-abutment piles," *Journal of Structural Engineering*, vol. 117, no. 7, pp. 2117–2134, 1991.

[9] L. Greimann and A. M. Wolde-Tinsae, "Design model for piles in jointless bridges," *Journal of Structural Engineering*, vol. 114, no. 6, pp. 1354–1371, 1988.

[10] R. E. Abendroth, L. F. Greimann, and P. B. Ebner, "Abutment pile design for jointless bridges," *Journal of Structural Engineering*, vol. 115, no. 11, pp. 2914–2929, 1989.

[11] A. T. Ghalesari, A. Barari, P. F. Amini, and L. B. Ibsen, "The settlement behavior of piled raft interaction in undrained soil," in *Proceedings of the IACGE 2013: Challenges and Recent Advances in Geotechnical and Seismic Research and Practices*, pp. 605–612, Chengdu, China, October 2013.

[12] A. T. Ghalesari, A. Barari, P. F. Amini, and L. B. Ibsen, "Development of optimum design from static response of pile–raft interaction," *Journal of Marine Science and Technology*, vol. 20, no. 2, pp. 331–343, 2015.

[13] M. R. Kamel, J. V. Benak, M. K. Tadros, and M. Jamshidi, "Prestressed concrete piles in jointless bridges," *PCI Journal*, vol. 41, no. 2, pp. 56–67, 1996.

[14] O. F. Yalcin, "A comparative study of live load distribution in skewed integral and simply supported bridges," *KSCE Journal of Civil Engineering*, vol. 21, no. 3, pp. 937–949, 2017.

[15] M. Modarresi, H. Rasouli, A. T. Ghalesari, and M. H. Baziar, "Experimental and numerical study of pile-to-pile interaction factor in sandy soil," *Procedia Engineering*, vol. 161, pp. 1030–1036, 2016.

[16] H. Krawinkler and G. D. P. K. Seneviratna, "Pros and cons of a pushover analysis of seismic performance evaluation," *Engineering Structures*, vol. 20, no. 4–6, pp. 452–464, 1998.

[17] S. A. Freeman, "Evaluations of existing buildings for seismic risk-a case study of Puget Sound Naval Shipyard," in *Proceedings of the 1st US National Conference on Earthquake Engineering*, pp. 113–122, Bremerton, WA, USA, 1975.

[18] D. M. Barbieri, "Two methodological approaches to assess the seismic vulnerability of masonry bridges," *Journal of Traffic and Transportation Engineering (English Edition)*, vol. 6, no. 1, pp. 49–64, 2019.

[19] I. M. E. El-Arab, "Soil structure interaction effects on pushover analysis of short span RC bridges," *Open Journal of Civil Engineering*, vol. 7, no. 3, pp. 348–361, 2017.

[20] R. Abbasnia, A. Tajik Davoudi, and M. M. Maddah, "An improved displacement-based adaptive pushover procedure based on factor modal combination rule," *Earthquake Engineering and Engineering Vibration*, vol. 13, no. 2, pp. 223–241, 2014.

[21] M. Bosco, A. Ghersi, E. M. Marino, and P. P. Rossi, "Comparison of nonlinear static methods for the assessment of asymmetric buildings," *Bulletin of Earthquake Engineering*, vol. 11, no. 6, pp. 2287–2308, 2013.

[22] R. S. Abeysinghe, E. Gavaise, M. Rosignoli, and T. Tzaveas, "Pushover analysis of inelastic seismic behavior of Greveniotikos bridge," *Journal of Bridge Engineering*, vol. 7, no. 2, pp. 115–126, 2002.

[23] R. K. Goel and A. K. Chopra, "Role of higher-"mode" pushover analyses in seismic analysis of buildings," *Earthquake Spectra*, vol. 21, no. 4, pp. 1027–1041, 2005.

[24] D. Dong, J. Hou, L. Xiao, and X. An, "Comparative study on the properties of common steel bars used in construction engineering at home and abroad," *Building Materials and Decoration*, vol. 15, p. 49, 2016.

[25] Z. Y. Xu, *Mountain Torrents and Prevention*, Water Conservancy Press, Beijing, China, 1979, in Chinese.

[26] S. Arsoy, J. M. Duncan, and R. M. Barker, "Behavior of a semiintegral bridge abutment under static and temperature-induced cyclic loading," *Journal of Bridge Engineering*, vol. 9, no. 2, pp. 193–199, 2004.

[27] B. C. Chen, Y. Z. Zhuang, and B. Bruno, *Joinless Bridge*, People's Communications Press of China, Beijing, China, 2013, in Chinese.

[28] D.-P. Kontoni and A. Farghaly, "3D FEM analysis of a pile-supported riverine platform under environmental loads incorporating soil-pile interaction," *Computation*, vol. 6, no. 1, p. 8, 2018.

[29] Z. P. Ling and J. W. Yi, *Foundation Engineering*, People's Communications Press of China, Beijing, China, 1997, in Chinese.

[30] J. X. Hong and D. W. Peng, "Computational model research of bridge without expansion joints," *China Journal of Fujian Architecture*, vol. 1, no. B10, pp. 56–58, 2001, in Chinese.

[31] J. X. Hong and D. W. Peng, "Research on the mechanical behavior of the integral abutment bridge with pile foundation," *China Journal of Highway*, vol. 15, no. 4, pp. 43–48, 2002, in Chinese.

[32] Institute of China Highway Planning and Design (ICHPD), *General Specifications for Design of Highway Bridges and Culverts: JTG D60-2015*, People's Communications Press of China, Beijing, China, 2015, in Chinese.

[33] Ministry of Transport of the People's Republic of China, *Load Test Method for Highway Bridge*, China Communications Press, Beijing, China, 2015.

[34] Institute of China Highway Planning and Design (ICHPD), *Specifications for Design of Highway Reinforced Concrete and Prestressed Concrete Bridges and Culverts: JTG3362-2018*, People's Communications Press of China, Beijing, China, 2018, in Chinese.

[35] Y. F. Chen, "Important considerations, guidelines, and practical details of integral bridges," *Journal of Engineering Technology*, vol. 14, no. 1, pp. 16–19, 1997.

[36] Institute of China Highway Planning and Design (ICHPD), *Specifications for Design of Foundation of Highway and Culverts: JTG D63-2019*, People's Communications Press of China, Beijing, China, 2019, in Chinese.

[37] J. L. Jorgenson, "Behavior of abutment piles in an integral abutment in response to bridge movements," *Transportation Research Record: Journal of the Transportation Research Board*, no. 903, pp. 72–79, 1983.

[38] K. Rollins and S. Jessee, "Passive force-deflection curves for skewed abutments," *Journal of Bridge Engineering*, vol. 18, no. 10, pp. 1086–1094, 2013.

[39] C. Pantelides, L. Ibarra, Y. Wang, and A. Upadhyay, *Seismic Rehabilitation of Skewed and Curved Bridges Using a New Generation of Buckling Restrained Braces*, Mountain Plains Consortium, Fargo, ND, USA, 2016.

[40] P. Kaviani, F. Zareian, and E. Taciroglu, "Seismic behavior of reinforced concrete bridges with skew-angled seat-type abutments," *Engineering Structures*, vol. 45, pp. 137–150, 2012.

[41] Y. Wang, L. Ibarra, and C. Pantelides, "Collapse capacity of reinforced concrete skewed bridges retrofitted with buckling-restrained braces," *Engineering Structures*, vol. 184, pp. 99–114, 2019.

[42] D. G. Gao, *Highway Bridge and Culvert Design Manual: Design of Bridge Site*, 2011.

[43] Z. Wang, J. Q. Wang, and J. Z. Zhu, "Pushover analysis of precast segmental UHPFRC bridge columns with unbonded posttensioned tendons," *Key Engineering, Materials*, vol. 765, pp. 391–396, 2018.

[44] G. W. Sun, "Seismic calculation of high-speed railway,"Master dissertation, Shijiazhuang Tiedao University, Shaoxing, China, 2013.

[45] A. Sahraei and F. Behnamfar, "A drift pushover analysis procedure for estimating the seismic demands of buildings," *Earthquake Spectra*, vol. 30, no. 4, pp. 1601–1618, 2014.

[46] F. L. Chen, "Evaluation of seismic performance of Y shape pier rigid frame bridge based on pushover method," *China Journal of Urban Bridge and Flooding Prevention*, vol. 3, pp. 61–64, 2019, in Chinese.

[47] Z. X. Peng, "Vulnerability analysis and evaluation of pile group foundation bridge under flood loading,"Master dissertation, Southwest Jiaotong University, Chengdu, China, 2017.

[48] H. F. Chen and L. Duan, *Seismic Design of Bridge Engineering*, China Machine Press, Beijing, China, 2008, in Chinese.

[49] M. R. Falamarz-Sheikhabadi and A. Zerva, "Effect of numerical soil-foundation-structure modeling on the seismic response of a tall bridge pier via pushover analysis," *Soil Dynamics and Earthquake Engineering*, vol. 90, pp. 52–73, 2016.

[50] J. B. Mander, M. J. N. Priestley, and R. Park, "Theoretical stress-strain model for confined concrete," *Journal of Structural Engineering*, vol. 114, no. 8, pp. 1804–1826, 1988.

[51] J. B. Mander, M. J. N. Priestley, and R. Park, "Observed stress-strain behavior of confined concrete," *Journal of Structural Engineering*, vol. 114, no. 8, pp. 1827–1849, 1988.

[52] R. Park and T. Paulay, *Reinforced Concrete Structures*, John Wiley & Sons, Hoboken, NJ, USA, 1975.

[53] T. Zordan, B. Briseghella, and C. Lan, "Parametric and pushover analyses on integral abutment bridge," *Engineering Structures*, vol. 33, no. 2, pp. 502–515, 2011.